

DESIGN OF AN OUTDOOR WIRELESS LOCAL AREA NETWORK AND
ANTENNA ANALYSIS

Except where reference is made to the work of others, the work described in this thesis is my own or was done in collaboration with my advisory committee. This thesis does not include proprietary or classified information.

Suzanne Oudit

Certificate of Approval:

Stuart M. Wentworth
Associate Professor
Electrical and Computer Engineering

Lloyd S. Riggs, Chair
Professor
Electrical and Computer Engineering

Zebediah Whitehead
Information Technology Specialist III
Engineering Network Services

Stephen L. McFarland
Dean
Graduate School

DESIGN OF AN OUTDOOR WIRELESS LOCAL AREA NETWORK AND
ANTENNA ANALYSIS

Suzanne Oudit

A Thesis

Submitted to

the Graduate Faculty of

Auburn University

in Partial Fulfillment of the

Requirements for the

Degree of

Master of Science

Auburn, Alabama
August 7, 2006

DESIGN OF AN OUTDOOR WIRELESS LOCAL AREA NETWORK AND
ANTENNA ANALYSIS

Suzanne Oudit

Permission is granted to the Auburn University to make copies of this thesis at its discretion, upon the request of individuals or institutions and at their expense. The author reserves all publication rights.

Signature of Author

Date of Graduation

VITA

Suzanne A. N. Oudit, daughter of Ian Oudit and Viola (Ramsaran) Oudit, was born on October 11, 1980 in San Fernando, Trinidad, West Indies. She graduated in May 2002 from the University of the West Indies (U.W.I), St. Augustine with a Bachelor's of Science in Electrical and Computer Engineering. She then joined the Electrical Engineering department of Auburn University as a graduate student in January 2004.

THESIS ABSTRACT

DESIGN OF AN OUTDOOR WIRELESS LOCAL AREA NETWORK AND

ANTENNA ANALYSIS

Suzanne Oudit

Master of Science, August 7, 2006
(BSc. University of the West Indies, 2002)

80 Typed Pages

Directed by Lloyd S. Riggs

One of the ongoing projects of the Engineering Network Services (ENS) at Auburn University (AU) is to design and implement an outdoor Wireless Local Area Network (WLAN). This project involved using Access Points (AP) that are provided by Meru Networks. The AU College of Engineering is acting as the test bed for the proposed AU WLAN. This thesis provides detailed documentation of the considerations involved in the implementation of the WLAN.

Another aspect of the project dealt with the analysis of WLAN antennas. Theoretical antenna radiation models were created and compared with the same from manufacturer's data sheets. A commercial cellular antenna manufactured by CSA Wireless was investigated. As part of the study of the CSA Wireless antenna, a patch antenna was fabricated and its performance characterized.

Outdoor field measurements were conducted in the vicinity of the AP and the results obtained were compared to the general antenna coverage patterns.

ACKNOWLEDGEMENTS

I would like to thank God for guiding me and giving me the encouragement, strength and will to pursue my goal in accomplishing this project and have the pleasure to see it terminate fruitfully when at times the struggle seemed as though it would never end.

To Dr. Lloyd Riggs, my project supervisor, a special thanks to him for his concern, support and guidance throughout this exercise and for having the faith in me to execute a successful project. To Dr. Michael Baginski who suggested and made arrangements for me to do work with the Engineering Network Services, Auburn University. To Dr. Stuart Wentworth for assisting me conduct some measurements.

In my efforts to achieve overall success, there were some special individuals who contributed significantly and who I would like to thank sincerely. These are: Dr. Daniel Faircloth, Mr. Zebediah Whitehead, Mr. Jitendra Palasagaram and Mr. Joe Haggerty.

To my parents, Ian and Viola Oudit, an extraordinary acknowledgement to them for being supportive and keeping the faith at all times.

Style manual of journal used Graduate School: Guide to preparation and submission of
theses and dissertations

Computer software used: Microsoft Office XP

TABLE OF CONTENTS

LIST OF FIGURES	xi
LIST OF TABLES	xiii
CHAPTER 1: INTRODUCTION	1
CHAPTER 2: CHARACTERIZATION OF THE WIRELESS CHANNEL	4
2.1 THE PROPAGATION ENVIRONMENT	4
2.2 INVESTIGATING MULTIPATH INTERFERENCE	5
2.3 LARGE SCALE PATH LOSS	6
2.3.1 Path Loss Propagation Model	6
2.3.2 Log-Distance Propagation Loss Model	8
2.3.3 Walfisch/Ikegami COST 231 Propagation Model	8
2.4 EXAMINING THE MODELS	10
CHAPTER 3: DESIGN APPROACH FOR OUTDOOR WLAN	11
3.1 SITE SURVEY	11
3.2 CHOICE OF EQUIPMENT	13
3.2.1 SA24-120-9 Sectored Antenna	13
3.2.2 Yagi Antenna: WISP24015PTNF 2.4 to 2.5GHz	14
3.2.3 Calculations For Antenna Downtilt	14
3.2.4 Antenna And AP Configuration	15
3.2.5 Access Point: Meru AP200	15
3.2.6 Meru Controller	17
3.2.7 Clinometer	18
3.2.8 PoE Injector	18
3.2.9 Wiring Description	18
3.2.10 WLAN Cable: LMR400	20
3.3 WLAN NETWORK DESIGN	20
3.3.1 AP Redundancy	21
3.3.2 Using Two Rather Than One AP	21
3.4 MAC AND SSID ASSIGNMENTS	22
CHAPTER 4: WLAN SECURITY	24
4.1 SSID	24

4.2 UNDERSTANDING THE IMPLEMENTATION OF SECURITY IN THE AU NETWORK BASED UPON CISCO’S CONFIGURATION	24
4.2.1 What is Cisco Clean Access?.....	24
4.2.2 Cisco Clean Access Components.....	25
4.3 THE AUTHENTICATION PROCESS	26
4.4 VPN.....	27
CHAPTER 5: OUTDOOR MEASUREMENTS.....	28
5.1 SIGNAL STRENGTH READINGS TO PREDICT AP COVERAGE.....	28
5.2 MEASUREMENTS PROCEDURE.....	28
5.3 BUILDING HEIGHTS TO PREDICT COVERAGE RANGE.....	30
CHAPTER 6: A THEORETICAL ANALYSIS OF AP AND ANTENNA COVERAGE	33
6.1 USING MALTBAB TO PLOT THE MANUFACTURER’S DATA.....	33
6.2 DEVELOPING A THEORETICAL MODEL.....	34
6.3 VERIFICATION TEST	36
6.3.1 Contour Plots Of Far-Field Radiation Pattern For SA24-120-9 Antenna.....	39
6.4 COORDINATE ROTATION AND TRANSLATION	40
6.5 COMPARING THE ANALYTICAL AND MEASURED PLOTS	42
CHAPTER 7: ANTENNA ANALYSIS: CREATING THE RADIATION PATTERN FOR THE CELLULAR ANTENNA.....	44
7.1 BACKGROUND	45
7.2 DETERMINING THE SINGLE ELEMENT FUNCTIONS.....	46
7.3 DETERMINING THE ARRAY FACTOR FUNCTION	47
7.4 CORRECTION FACTOR	48
7.5 RESULTS OF PATTERN MULTIPLICATION	48
CHAPTER 8: GENERAL ANALYSIS OF THE INPUT IMPEDANCE CHARACTERISTIC	51
8.1 BACKGROUND	51
8.2 ANALYZING THE PCSS090-10-0 ANTENNA.....	52
8.2.1 Using The VNA	52
8.3 BUILDING THE MICROSTRIP PATCH AND CONDUCTING MEASUREMENTS.....	55
8.4 SMITH CHART ANALYSIS.....	56
8.4.1 Smith Chart Of PCSS090-10-0 Antenna	57
8.4.2 Commercial Board Antenna Smith Chart	59
8.5 COMPARING A THEORETICAL VALUE OF IMPEDANCE TO THE MEASURED VALUE	60
8.6 SUMMARY	60
CONCLUSION.....	62
RECOMMENDATIONS.....	64
REFERENCES	66

LIST OF FIGURES

Figure 2.1 Graph of multipath interference for Broun AP.....	5
Figure 2.2 Graph of multipath interference for APa1.....	6
Figure 2.3 Comparing the theoretical models with measured data.....	10
Figure 3.1 Proposed coverage area.....	12
Figure 3.2 Flow diagram of site selection.....	13
Figure 3.3 Figure showing how the downtilt coverage was calculated.....	14
Figure 3.4 Frequency and Channel assignment in the United States.....	16
Figure 3.5 Example of 802.11b channel allocation.....	16
Figure 3.6 All of meru's APs on channel 6.....	17
Figure 3.7 Diagram depicting Meru's Virtual AP.....	17
Figure 3.8 PoE to backbone wiring configuration.....	19
Figure 3.9 Network Diagram of the WLAN to the wired LAN.....	21
Figure 4.1 Cisco's method for getting onto the network.....	25
Figure 4.2 Flow diagram showing what is taking place at Perfigo.....	26
Figure 4.3 VPN associated with WLAN.....	27
Figure 5.1 Variation of signal strength from Broun Hall's AP.....	29
Figure 5.2 Variation of signal strength from the APs for Aerospace- APa1 (upper plot), APa2 (lower plot).....	30
Figure 6.1 Polar plot generated in matlab based on raw data for (a) H-plane (b) E-plane	34
Figure 6.2 3D Coordinate orientation for the analysis below.....	34
Figure 6.3 Manufacturer's data (red) overlaid with the model (blue) for radiation patterns a) Elevation, m b) Horizontal, n.....	36
Figure 6.4 Coordinate system relative to exact geographic measurements.....	37
Figure 6.5 Process for creating Figures 6.6 and 6.7.....	38
Figure 6.6 Contour plot of a radiation pattern with equal E and H-plane half power beamwidth.....	38
Figure 6.7 Contour of the antenna for field pattern.....	39
Figure 6.8 Comparing the original axes with the new ones after a 20° downtilt or rotation	40
Figure 6.9 Ground plot after translation and rotation.....	42
Figure 6.10 Empirical results for Broun Hall antenna's ground coverage.....	43
Figure 7.1 PCSS090-10-0 6-element microstrip patch antenna.....	44
Figure 7.2 3D coordinate system for PCSS090-10 antenna.....	46
Figure 7.3 H-plane pattern multiplication.....	49
Figure 7.4 E-plane pattern multiplication.....	50

Figure 8.1 PCSS090-10-0 antenna connected to VNA.....	52
Figure 8.2 VSWR vs. Frequency for a matched load	53
Figure 8.3 VSWR vs. Frequency for the PCSS090-10-0 antenna inside radome.....	54
Figure 8.4 VSWR vs. Frequency for the PCSS090-10-0 antenna outside radome.....	55
Figure 8.5 (a)Fabricated patch based upon commercial cellular patch (b)SMA connector used to provide an edge-feed to the patch.....	56
Figure 8.6 Smith Chart of PCSS090-10-0 outside radome.....	57
Figure 8.7 Smith Chart of PCSS090-10-0 inside radome.....	58
Figure 8.8 Smith Chart of commercial board antenna.....	59
Figure 8.9 Examples of matching alterations	61

LIST OF TABLES

Table 3.1 ESSID and MAC addresses of the APs	23
Table 5.1 Buildings' height where the APs were located.....	31
Table 5.2 Inner and outer radius calculations for the three APs based on [1]	31

CHAPTER 1: INTRODUCTION

ENS is attempting to improve their wireless service to engineering students. Once satisfactory results are obtained, outdoor service will be provided campus-wide. The ultimate goal is to have Auburn University act as a host site providing wireless networking service, both audio and data, to the city of Auburn and possibly to its city limits. Similar work is already being conducted at other universities. Currently, the University of Georgia is coordinating an outdoor WLAN project “throughout 24 blocks of downtown Athens that will be used to research and explore applications for wireless technology in a real-world environment” [11].

Broadband connectivity is available in all buildings via Ethernet cabling but the coverage provided by these systems is far from ubiquitous. The importance of such an outdoor wireless system is to allow users untethered network access that would not confine them within the walls of their department. It is desirable for the campus network to grow geographically larger while still retaining efficiency and speed.

When deploying a WLAN, the cost, coverage and capacity must be evaluated and depends among other things on the frequency of operation. The network designer strives to minimize costs but at the same time provide quality service to the user and achieving their goals usually is not readily attainable without a compromise. In short, network designers usually try to create a system that accommodates as many users as possible

without jeopardizing service. In the planning phase of the WLAN, the designers should choose equipment that can be easily scaled to support anticipated applications like streaming video.

Once the WLAN is successfully deployed, it can be used by faculty and students to perform innovative wireless research and tests for mobile media design that could be integrated into the degree curriculum and push AU to the forefront of a fascinating research area.

Antenna analysis requires one to not only have a good understanding of antenna theory but also to be able to manipulate 3D geometry in both the Cartesian and spherical coordinate systems and furthermore carry out simulations, interpret, and compare results to the manufacturer's data sheet.

This document is divided into chapters that follow in roughly chronological order the steps taken to analyze the proposed WLAN. The two main concentrations in this thesis are the WLAN design and the antenna analysis.

Chapter 2 presents plots of multipath interference in order to demonstrate that the multipath channel has small scale fading and is random. Existing empirical large-scale models developed for various environments are compared with the outdoor measurements conducted.

Chapter 3 is the beginning phase of the WLAN design. Once a site survey is completed, it is very necessary to choose the equipment to be used in the design. The individual components are chosen based on their functionality and the service they provide to the overall system. Here, one is presented with the WLAN's hardware architecture. The Media Access Control (MAC) and Service Set Identifier (SSIDs) are

used to identify the specific AP that is under test and differentiates it from other AP signals present.

A wireless system is generally not as secure as its wired counterpart. The focus of Chapter 4 is to investigate different possible security measures. Several levels of hardware and software security were necessary in order to maintain privacy and security for the users, and to protect network resources and equipment.

As discussed in Chapter 5, once the AP and antenna was mounted, the signal strength had to be measured to determine the range of coverage offered by the chosen location. Matlab plots are used to provide a visual representation of the coverage area. Given the mounting height of the antenna, the antenna's downtilt angle was chosen to achieve the best ground coverage.

In Chapter 6 the ground coverage pattern of a candidate AP design is investigated. In particular, the radiation patterns specified by Pacific Wireless for the SA24-120-9 sectored antenna are examined in some detail.

In Chapter 7 the radiation pattern of a cellular phone transmitting antenna is derived by applying a technique referred to as *Pattern Multiplication* [13]. Again, theoretical results are compared to that of published data from the manufacturer.

In Chapter 8, further analysis of the base-station antenna, PCSS090-10-0 from Chapter 7 is conducted. An attempt is made to achieve a deeper understanding of how the input impedance of a single isolated patch was related to the same for the six-patch antenna. The analysis is based on measured Voltage Standing Wave Ratio (VSWR) values and Smith Chart plots.

CHAPTER 2: CHARACTERIZATION OF THE WIRELESS CHANNEL

Chapter 2 mentions factors that cause impairments in the wireless channel. Existing empirical models are introduced and compared with the actual measured data to see which model most closely represents the environment in which the AU WLAN would operate. In order to plan AP layout, theoretical models were used to predict signal attenuations or coverage of the proposed WLAN.

2.1 THE PROPAGATION ENVIRONMENT

Corruptive elements distort the information-carrying signal as it penetrates the propagation medium between the transmitter and receiver in an outdoor environment. The corruptive elements along the electromagnetic path are in the form of multipath delay spread, reflections, scattering, diffraction and penetration.

Small-scale fading is used to describe the rapid fluctuations of the amplitudes, phases or multipath delays of a radio signal over a short period of time or travel distance, so that the large-scale path loss effects may be ignored. Large-scale fading models try to predict the signal strength for an arbitrary Transmitter-Receiver, T-R separation typically hundreds or thousands of meters [10].

2.2 INVESTIGATING MULTIPATH INTERFERENCE

At a fixed location several readings were taken in one minute intervals for twenty minutes. The signal strengths (dBm) at the receiver are plotted as a function of time (min) to examine multipath interference.

It can be seen from Figures 2.1 and 2.2 that at each AP location that the signal strength fluctuated. This implied that as the radio signal radiated from the AP, it bounced off objects in the environment causing multiple propagation paths. The various signals arriving at the receiver interfere. Hence, the higher signal strength values correspond to more constructive interference while lower values correspond to destructive interference.

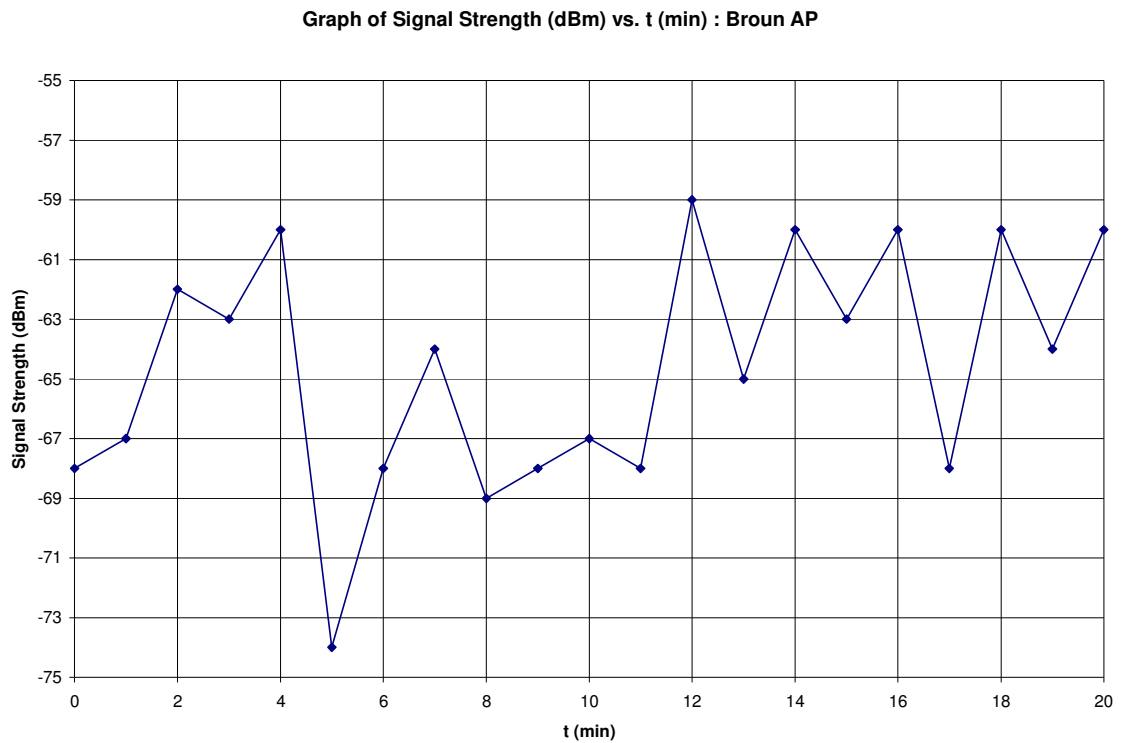


Figure 2.1: Graph of multipath interference for Broun AP

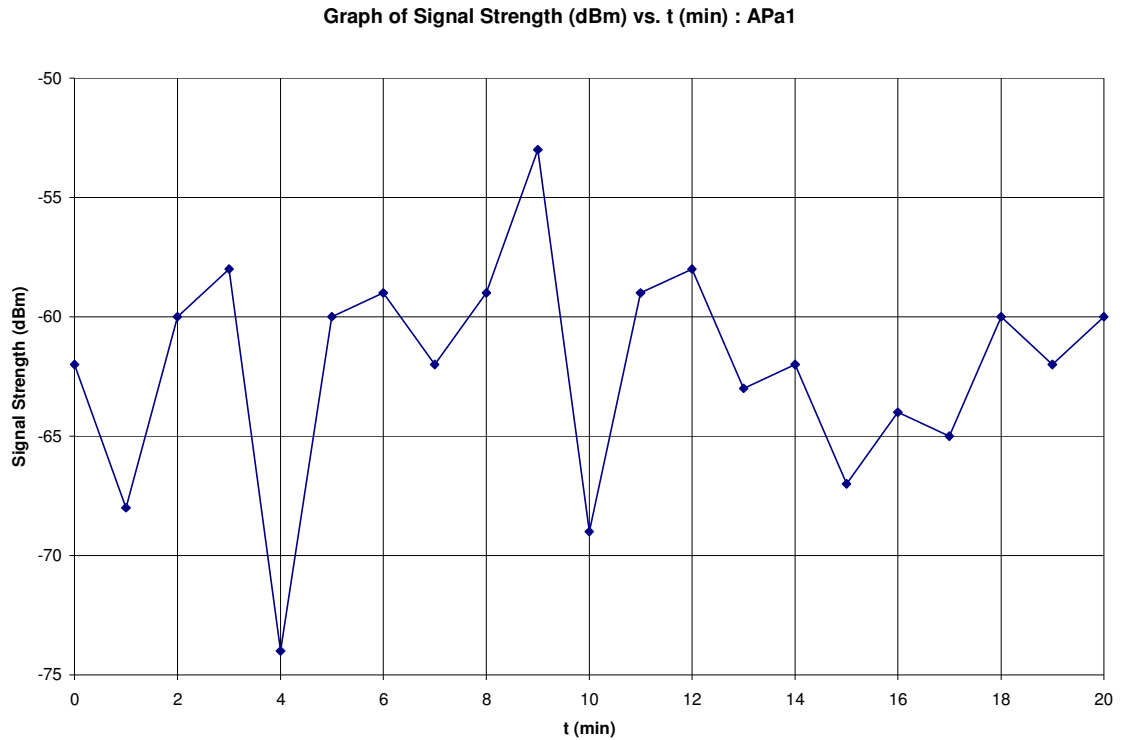


Figure 2.2: Graph of multipath interference for APa1

2.3 LARGE SCALE PATH LOSS

Large scale propagation models characterize the gradual fluctuations of the received signal strength over large distances. One will next see how large scale propagation models are used to predict received signal power in the designed wireless communication system.

2.3.1 Path Loss Propagation Model

According to feedback from the technical support team at MAXRAD, the transmitter's output power is defined as, "ERP is based on the output power of the radio subtract

jumper loss to the antenna plus antenna gain.” Based on this, the Effective Radiated Power is given by,

$$ERP = P_{tx} - L_c + G_A \quad (2.1)$$

where the transmitter output power, P_{tx} is -10dB, the SA24-120-9 antenna gain, G_A is 9dB and the LMR400 cable loss, L_c , is the loss per meter (0.2dB/m [17]) plus the connection loss (0.2dB). Since the length of LMR400 cable was approximately four feet (1.2192m), the cable loss was estimated per meter. Considering these values in equation 2.1 yields $ERP = -1.4\text{dB}$ or 28.6dBm.

The Free Space Path Loss (FSPL) propagation model is used to predict the received signal strength when the transmitter and receiver have a clear, unobstructed LOS path between them. It is impossible to specify performance for all environments but the free space performance characteristics provide the most suitable reference for comparing relative antenna performance.

Using the FSPL equation [15],

$$PL(d) = 20\log_{10}f_c + 20\log_{10}d - 147.56 \text{ (dB)} \quad (2.2)$$

where the center frequency, $f_c = 2.4\text{GHz}$,

$$PL(d) = 40 + 20\log_{10}(d) \text{ (dB)} \quad (2.3)$$

In the plot of Figure 2.3, the received power for the FSPL model (transmitted power less the path loss) is compared to the measured data.

2.3.2 Log-Distance Propagation Loss Model

The average large scale path loss for an arbitrary T-R separation can be expressed as a function of the distance using a path loss exponent, n . Propagation models indicate that the average received signal power decreases logarithmically with distance, therefore

$$PL(d) \propto (d/d_0)^n \quad (2.4)$$

or

$$PL(\text{dB}) = PL(d_0) + 10n \log_{10}(d/d_0) \quad (2.5)$$

where PL is the path loss, d is the distance indicative of the T-R separation and d_0 is the close-in reference distance determined from measurements from the transmitter.

From the FSPL equation, where $PL = 40 + 20 \log_{10}(d_0)$ (dB), d_0 was set to 42m based on the empirical data. For free-space, the path loss exponent is 2 but for this application the propagation path was not entirely free space so n was set to 2.3. The Log-distance model plot is shown in Figure 2.3.

2.3.3 Walfisch/Ikegami COST 231 Propagation Model

The Walfisch/Ikegami COST 231 propagation model considers the impact of rooftops and building height by using diffraction to predict average signal strength at street level. The model considers the path loss to be a sum of three factors, free space loss (L_f), roof top to street diffraction and scatter loss (L_{rts}) and multiscreen loss (L_{ms}).

$$L_c(\text{dB}) = L_f(\text{dB}) + L_{rts}(\text{dB}) + L_{ms}(\text{dB}) \quad (2.6)$$

where

R = T-R separation 0.03048km to 0.213km

f_c = operating frequency, 2400MHz

W = street width, 5m

h_r = building height, 19.2m

h_m = mobile devices's height, 1.65m

ϕ = incident angle relative to the street, 20°

b = distance between buildings, 7m

are all parameters needed to compute L_c (dB) assuming that the building height exceeds the mobile height in a suburban area [9].

After inserting the values for all the parameters in equation 2.6, the result of the Walfisch/Ikegami COST 231 propagation model's path loss is,

$$L_c(\text{dB}) = 112.74 + 38\log_{10}(R) \quad (2.7)$$

The COST 231 propagation model's plot is shown in Figure 2.3.

2.4 EXAMINING THE MODELS

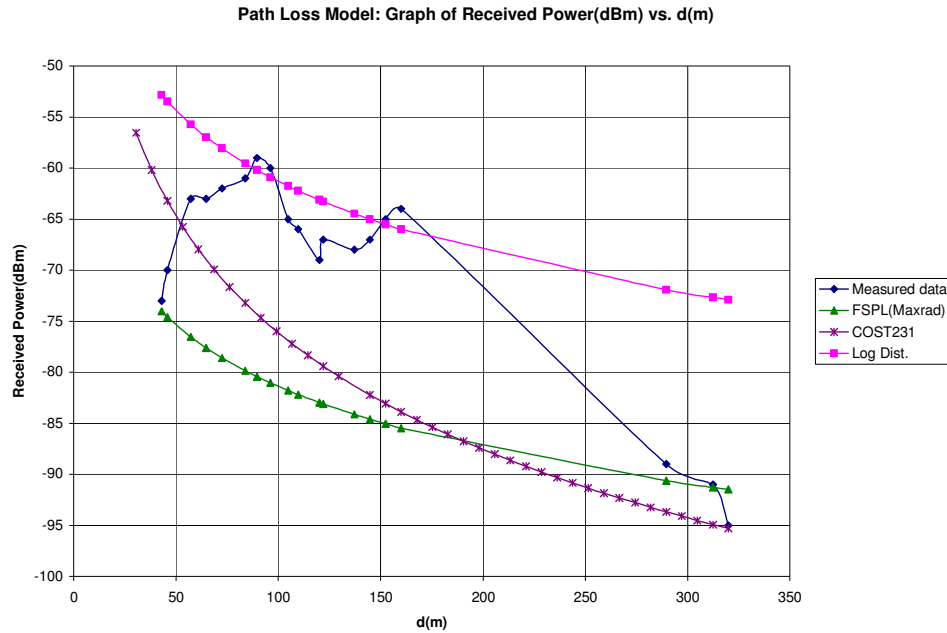


Figure 2.3: Comparing the theoretical models with the measured data

In Figure 2.3, the COST 231, FSPL and Log-Distance models are reasonably close to the measured data. Since the Log-Distance model is dependent on free space propagation, the match between the measured data and the model is appropriate as the measurements were taken in an open area.

The COST 231 model takes into account free space loss, multipath loss, diffraction and scatter loss. Factors were also included to accommodate for the type of environment i.e. mid-sized city and suburban area with moderate tree density or metropolitan center. Since the COST 231 took more factors into consideration when calculating the link budget, one can see that there is reasonably good agreement with the actual measurements. The overall conclusion is that all the models are reasonably consistent with the data.

CHAPTER 3: DESIGN APPROACH FOR OUTDOOR WLAN

Chapter 3 explains considerations made when designing a wireless network. It examines the equipment choice and performance and how the hardware is connected from the wireless side to the existing wired network backbone. One is also presented with the role of Media Access Control (MAC) addresses and Service Set Identifiers (SSID) that are assigned early in the design for later testing of the WLAN.

3.1 SITE SURVEY

On a map (Figure 3.1) of the engineering portion of campus, the areas that were to have wireless service were established. A site analysis was conducted to identify the best antenna positions for an optimum and seamless blanket of coverage. This task was done to minimize dead spots and identify those areas that would be receiving low powered signals and hence low bandwidth connections. Planning was essential in the early stages of the project so that troubleshooting in the later stages would require less effort. If there was any disruption in service, the user would not be wondering if his device or the AP or even the application server may be faulty. Figure 3.2 shows a flow diagram describing the method for determining the site selection.

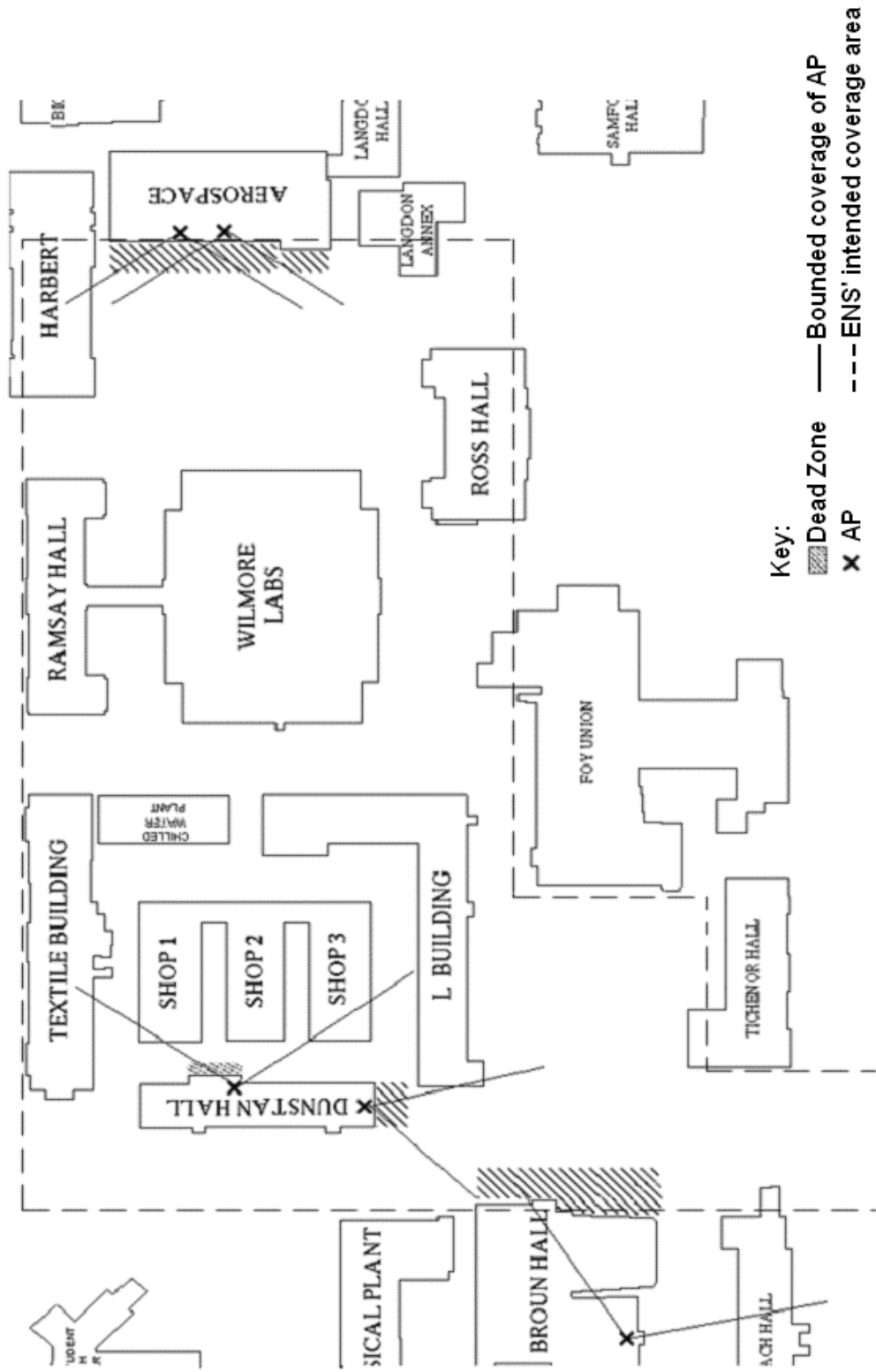


Figure 3.1: Proposed coverage area

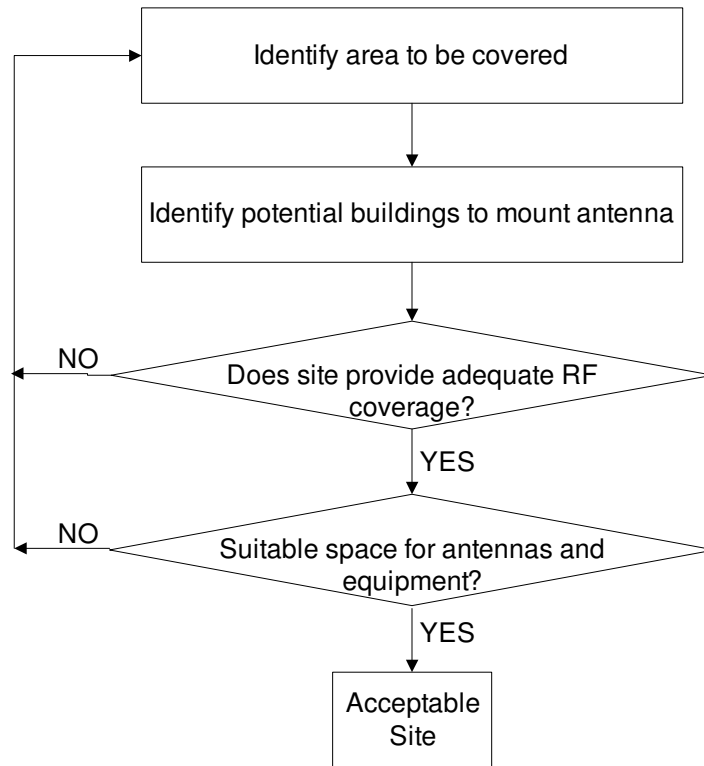


Figure 3.2: Flow diagram of site selection

3.2 CHOICE OF EQUIPMENT

3.2.1 SA24-120-9 Sectored Antenna

A directional antenna would cause minimum interference to the other transmitters and receivers plus a more focused beam would be achieved providing greater signal strength to the intended receiver. The selected sectored antenna, SA24-120-9, is manufactured by Pacific Wireless. This model was chosen since it had a large vertical beamwidth, 120° and could even operate at 180° sectoring if the system requirements were to change in the future, was compatible with 802.11b and 802.11g applications, was physically light and had a mechanical downtilt of 45°. The gain of this antenna was 9dBi. These were all desirable characteristics for choosing an antenna. This vertically polarized antenna was positioned on Broun Hall and two more on the Aerospace building.

3.2.2 Yagi Antenna: WISP24015PTNF 2.4 to 2.5GHz

The WISP24015PTNF is a product of PCTEL MAXRAD. The Yagi antenna was positioned on the roof of Dunstan Building since in the preliminary design phase, the intent was for this antenna to compensate for the dead spot directly in front of Broun Hall while providing additional coverage as far as possible along the Haley concourse. The befitting characteristics of this antenna in the WLAN would be its 30° horizontal beamwidth and its 15dBi gain.

3.2.3 Calculations For Antenna Downtilt

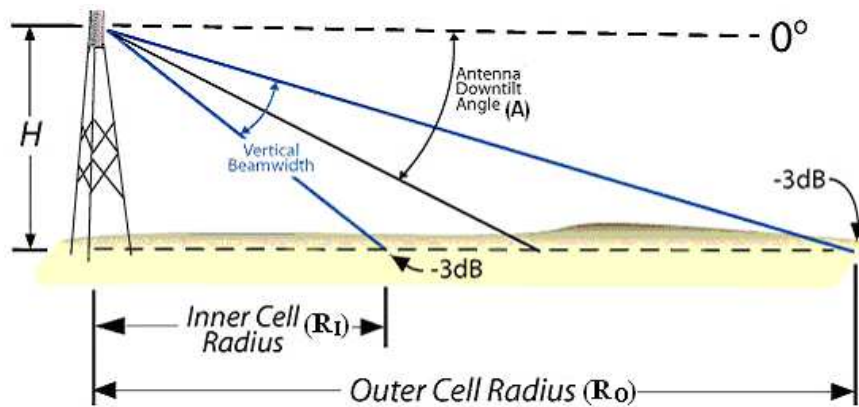


Figure 3.3: Figure showing how the downtilt coverage was calculated [1]

Basic geometrical analysis and calculations based on Figure 3.3 were performed to evaluate the antenna's downtilt. The antenna was tilted downwards in order to maximize ground coverage.

As an example, the height, H of the Aerospace building would be used as the antenna's height, 75 feet. From the SA24-120-9 antenna's data sheet, the vertical beamwidth, BW , is 40° . Equations 3.1 and 3.2 below are used to compute the inner radius distance, R_I and the outer radius distance, R_O .

$$R_I \text{ (feet)} = H / \tan(A + (BW/2)) \quad (3.1)$$

$$R_O \text{ (feet)} = H / \tan(A - (BW/2)) \quad (3.2)$$

In the calculations, the downtilt angle, A was varied such that R_I was made a minimum value and R_O was made a maximum value to achieve a maximum antenna coverage area. R_O would be at a maximum (infinity) if the downtilt angle is a value equal to $BW/2$. Basically, the outer radius would be at 0° implying that the -3dB edge of the main lobe would also be at 0° . In the calculations, a value slightly higher than $BW/2$ was chosen.

3.2.4 Antenna And AP Configuration

The AP and antenna acted as one unit. If antenna positioning was not properly addressed, then the AP may not have been able to attain maximum effective range. The antenna operated like an “ear”, hearing the weaker signals and then transmitting an amplified response to the wireless device. See Figure 3.9 for the antenna and AP configuration.

3.2.5 Access Point: Meru AP200

2.4GHz and 5GHz band systems are not directly compatible. Not long ago one did not have to worry about operating in various frequency bands as only 802.11b (2.4GHz) products were available. Vendors however have been offering dual-band radio Network Interface Cards (NICs). Meru’s AP can accommodate 802.11a (5.8GHz), 802.11b and 802.11g clients thus diminishing the interoperability problem.

Figure 3.4 illustrates the frequency channel assignment in the United States for traditional 802.11b. If adjacent signal frequencies overlap, they could cause interference

problems in the system so non-overlapping channels like 1, 6 and 11 are used when in the vicinity of each other.

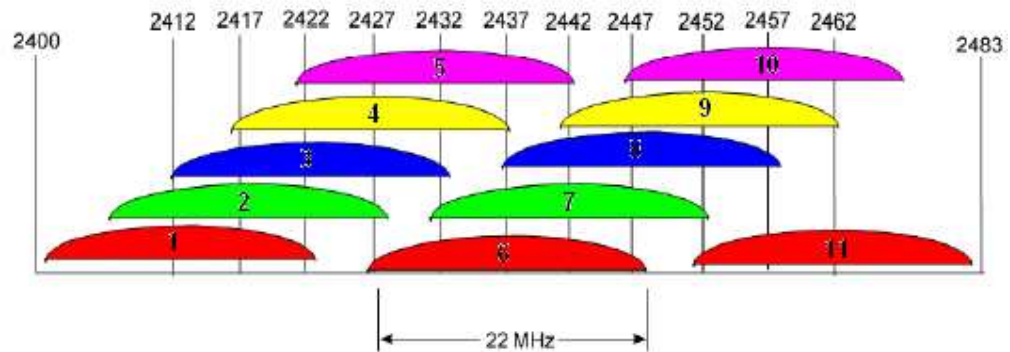


Figure 3.4: Frequency and Channel assignment in the United States [6]

In a real-life deployment of wireless APs, Figure 3.5 shows the selection of channels in a traditional 802.11b configuration where no two overlapping coverage cells have the same frequency.

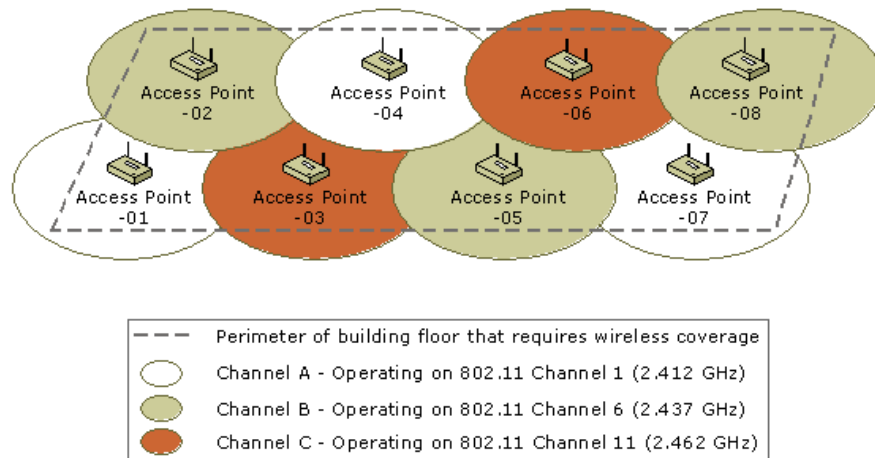


Figure 3.5: Example of 802.11b channel allocation [5]

Meru’s design allows the WLAN to use one frequency channel shared among all other APs [5] to provide seamless connectivity to the client. According to the Meru configuration, all APs operate on channel six (2.428GHz to 2.450GHz) in the 2.4GHz

frequency spectrum for 802.11b and 802.11g as illustrated in Figure 3.6. This is a better design approach than traditional APs which would cause interference problems if the same channel were used rather than the channel 1, 6 and 11 assignments.

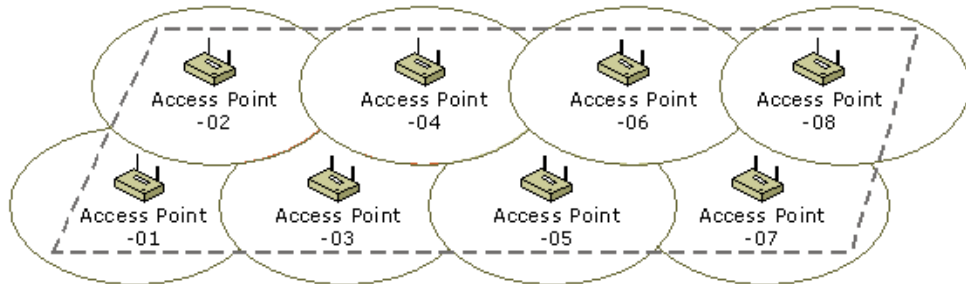


Figure 3.6: All of Meru's AP's on channel 6

Meru's technique of using a 'Virtual AP', allows multiple APs to function as a single cell to provide the transparent mobility that allows users to roam without interruption [8] as seen in Figure 3.7.

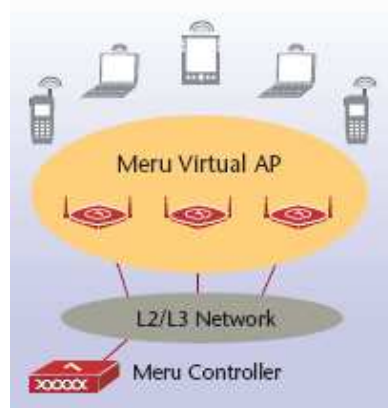


Figure 3.7: Diagram depicting Meru's Virtual AP

3.2.6 Meru Controller

The Meru Controller is a WLAN appliance that coordinates the APs and enforces all WLAN technologies including security, plug and play deployment, RF management,

mobility, contention management and Quality of Service, QoS. The controller is located on a Layer 3 switched network in Haley Center.

3.2.7 Clinometer

The meter used to measure the downtilt angle was a commercial clinometer. This measuring device was used to measure the angle of line-of-sight above or below the horizontal. It was also used to set the horizontal bearing (angle, cardinal direction) of the main lobe of the antenna.

3.2.8 PoE Injector

“802.3af is an IEEE standard for powering network devices via Ethernet cable. Also known as Power-over-Ethernet, it provides 48 volts over 4-wires” [4] of an eight wire data cable rather than have separate power cables for the operation of the AP. The PoE injector minimizes the number of wires that must be strung in order to install the network resulting in lower system costs, shorter downtime, easier maintenance and greater installation flexibility. See Figure 3.8 for PoE configuration.

3.2.9 Wiring Description

The diagram in Figure 3.8 indicates the wiring configuration from the PoE to the network’s backbone.

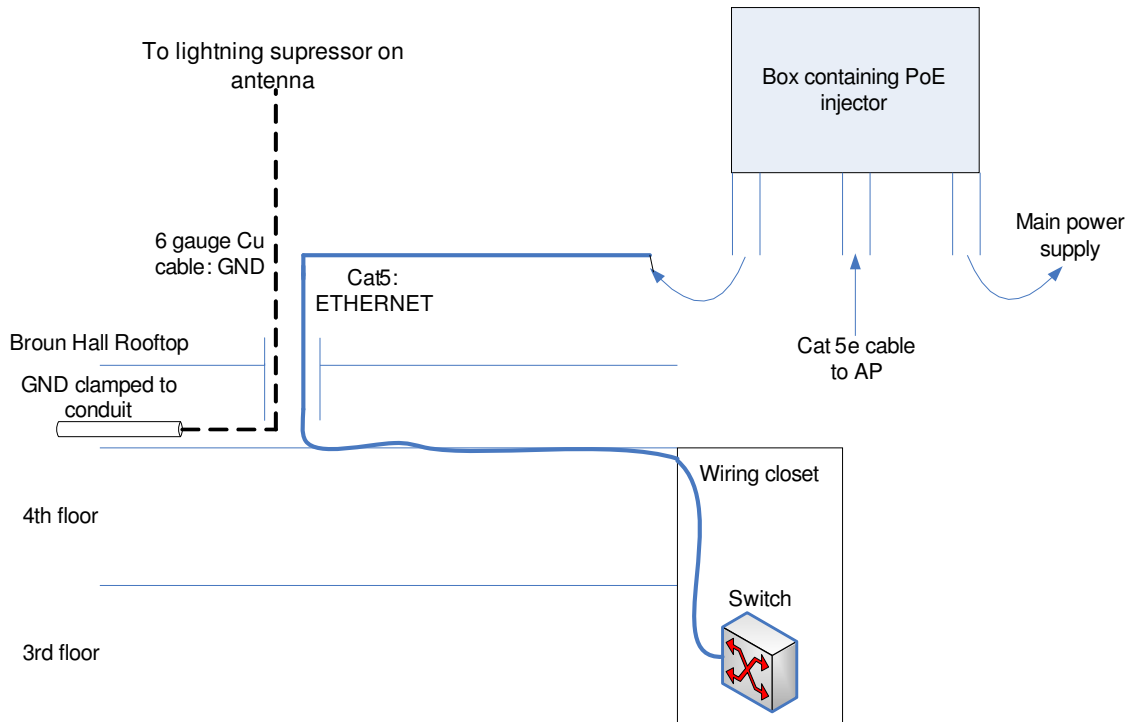


Figure 3.8: PoE to backbone wiring configuration

The NEMA 4 rated enclosure which housed the PoE injector had to be water resistant since it was positioned on the rooftop where it would be exposed to the weather. There were three ports on the box, one for a connection to the AP, one to the mains supply and the last to a switch in the wiring closet. The blue Ethernet cable (solid line) had a Cat5e Outdoor UV rating. The ground cable (broken line) from the lightning suppressor was clamped to an already grounded conduit running in the building. The network wiring configuration followed that of the TIA568A standard. This standard was used for the RJ45 jack at the connection of the Ethernet cable into the PoE box.

An Infrastructure mode was implemented as opposed to the Ad-Hoc mode. Ad-Hoc mode is simply peer-to-peer communication among wireless clients. In an Infrastructure

mode, all wireless clients connect through APs which are attached to switches on the wired backbone.

3.2.10 WLAN Cable: LMR400

LMR400 cable is suitable for WLAN applications. It was decided that less than four feet of LMR400 cable would be used to connect between the AP and antenna. The AP would then be placed outside the building using Cat5 cable from the AP to the switch. In this manner, the cable loss would be reduced to approximately 0.5dB.

3.3 WLAN NETWORK DESIGN

Figure 3.9 gives pictorial details of all the components and connections involved from the wireless side to the wired backbone. The 120° sectored antenna with its 20° downtilt has a lightning suppressor connected to its base to prevent any electrical surges propagating throughout the rest of the connected equipment. Besides powering the AP, the PoE injector allows the digital electrical signals to pass through to the wired backbone via the Cat5e cabling. After passing through a switch and router pair, one will then be able to gain access to the Internet.

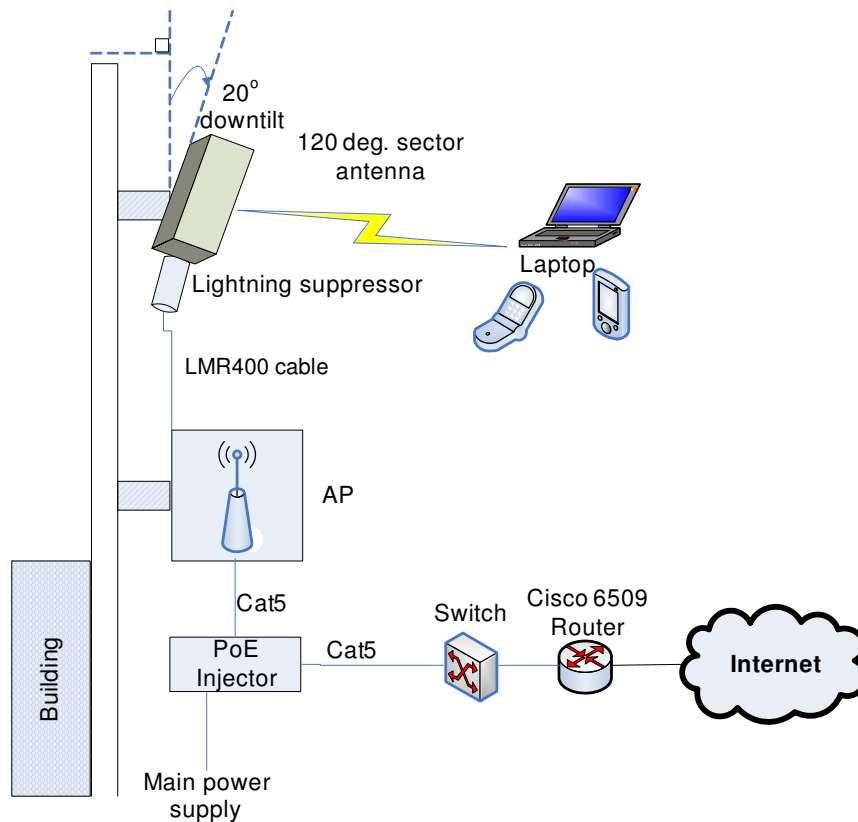


Figure 3.9: Network Diagram of the WLAN to the wired LAN to the Internet

3.3.1 AP Redundancy

There is no physical redundancy installed (ie. a backup AP) on the network, so that if one failed the other may come into effect for seamless operation and continuity of service to the user. There are “hot spares” though so that the old AP may be removed if it fails and a new one installed. Once this new AP comes online, the Meru Controller would transfer data from the old to the new AP via the management interface.

3.3.2 Using Two Rather Than One AP

It was decided to use two APs on the Aerospace building for improved network performance and reliability of client service. Some of the benefits shall be discussed. If

the network becomes saturated, one AP would not have to compromise service if the other is free. Load balancing could swap clients between APs. A single AP would receive all the noise from the environment or other wireless users but with two APs, the noise would be halved per AP. Two APs would double the capacity and be able to accommodate more traffic for that particular geographic location or support a client using a high bandwidth application.

3.4 MAC AND SSID ASSIGNMENTS

The public name of the WLAN is the SSID. All wireless devices on a WLAN must employ the same alpha-numeric SSID in order to communicate with each other. Table 3.1 shows the MAC addresses with their corresponding SSIDs.

It was quite helpful to have the SSIDs when taking signal strength measurements for the different APs to create the coverage plots in Matlab. Initially, a laptop equipped with Netstumbler, a network analyzer application, was used to acquire each AP's signal strength. The received signal displayed on Netstumbler was a combination of signals from different APs at that particular location. The problem arose when one could not differentiate the desired signal from the unwanted signals. To combat this problem, the handheld device (PDA) equipped with the AirMagnet software was used whereby one saw the signal strength for the particular AP based upon its SSID which was provided by the network administrator.

Table 3.1: ESSID and MAC addresses of the APs

MAC ADDRESS	LOCATION (ESSID)
000CE605531E	Aerospaceroof_1
000CE60A76DD	Aerospaceroof_2
000CE001ED5	Broun Roof

ENS made the hidden SSIDs available to the author for testing purposes. Generally, if one connected to the WLAN, one would be connecting to the valid SSID's of *Meru_Test* and *Tsunami*.

CHAPTER 4: WLAN SECURITY

Security is an essential component of a WLAN design. Since a wireless system is not as secure as a wired one, levels of security had to be included to prevent intruders from viewing, modifying or stealing a user's private information.

4.1 SSID

In the configuration used in the AU network, each AP advertises its presence to all wireless devices in range several times per second by broadcasting beacon frames that carry its SSID. One might ask, does the SSID provide network security? Since the SSID is being broadcasted, its plaintext can be sniffed by rogue clients but they may not enter the network unless they are authenticated via a username and password.

4.2 UNDERSTANDING THE IMPLEMENTATION OF SECURITY IN THE AU NETWORK BASED UPON CISCO'S CONFIGURATION [14]

4.2.1 What is Cisco Clean Access?

Cisco Clean Access is a powerful, easy to use network management and security solution. With comprehensive security features, user-authentication tools, and bandwidth and traffic-filtering controls, Cisco Clean Access is a complete solution for controlling

and securing the network all in one place rather than having to propagate the policies throughout the network on many devices.

4.2.2 Cisco Clean Access Components

The Clean Access Manager (CAM) is the administrative server for Clean Access deployment and the Clean Access Server (CAS) is the gateway server and enforcement engine between the untrusted and trusted network. The CAS enforces policies defined in the CAM admin console, including network access privileges, authentication requirements, bandwidth restrictions, and Clean Access system requirements. Figure 4.1 shows the role of the CAS and the CAM relative to a section of AU's network.

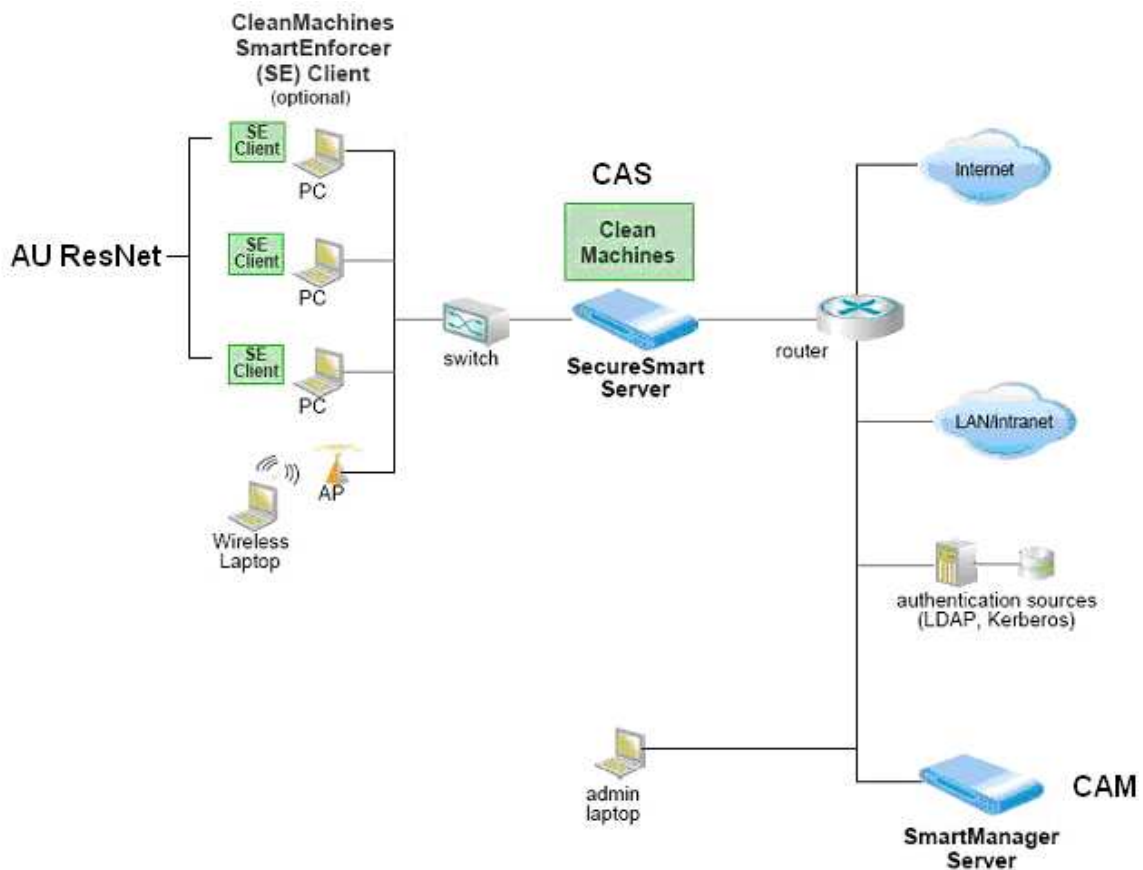


Figure 4.1: Cisco's method for getting onto the network [14]

4.3 THE AUTHENTICATION PROCESS

The wireless device recognizes the beacon signal from the Meru AP. Packets of data from the wireless device pass through the switch to the Perfigo box. The flow diagram in Figure 4.2 illustrates what occurs at Perfigo.

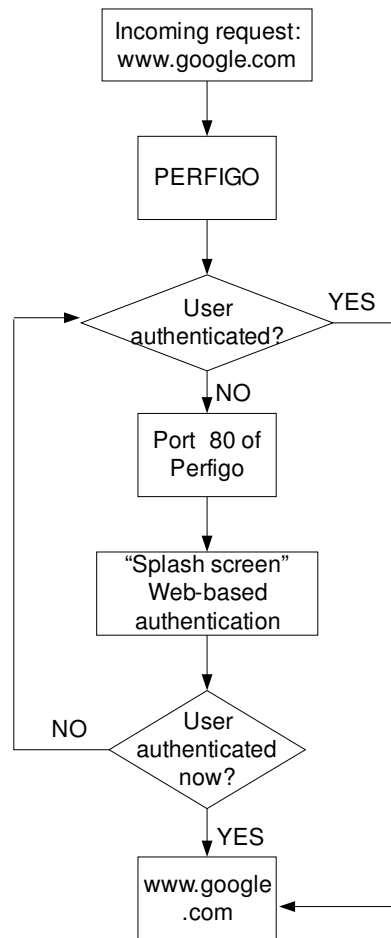


Figure 4.2: Flow diagram showing what is taking place at Perfigo

First time users are authenticated on the network by a web login page or “splash-screen”. This is the user’s side of Perfigo. When the Cisco CAS receives an HTTP request, it checks to see if the request came from an authenticated user. If not, a secure

login page is presented to the user. The login credentials can be authenticated by the CAM [14].

4.4 VPN

The VPN is one of Auburn's WLAN most effective security methods. It allows the network administrator to add a layer of encryption to plaintext protocols like *telnet*, *ftp* and *imap* just to name a few. Diagram 4.3 shows the encrypted VPN for accessing information relating to AU.

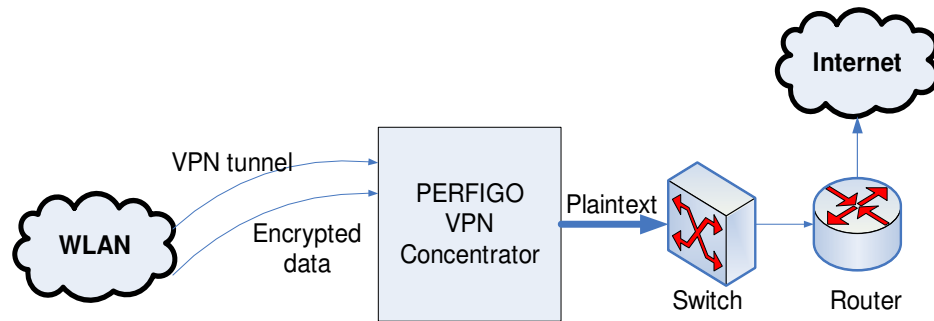


Figure 4.3: VPN associated with WLAN

CHAPTER 5: OUTDOOR MEASUREMENTS

Chapter 5 describes how antenna or field strength measurements were conducted and the equipment and material that were needed. Matlab plots of the field intensity measurements are included to indicate coverage areas.

5.1 SIGNAL STRENGTH READINGS TO PREDICT AP COVERAGE

Measurements were conducted on the AU campus where all the engineering schools were located. The materials used were a 25 feet Craftsman measuring tape and chalk. A Compaq iPAQ pocket PC equipped with the AirMagnet software and having a Cisco Aironet 350 wireless adapter was used to measure the received signal strength from the antenna.

5.2 MEASUREMENTS PROCEDURE

On a scaled map of the engineering campus, points were located at 50 feet intervals from each other. A cluster of points were identified that were located in the vicinity of the AP that was under test. At a particular test point, the pocket PC that contained the wireless card was held facing the AP. From the AirMagnet software, the known MAC addresses of the APs were found and the corresponding signal strength received (dBm)

was recorded. There were two APs, APa1 and APa2, on the Aerospace building and one on Broun Hall.

The Matlab software was used to create the plots whereby the signal strength of the AP could be examined as the wireless device was moved further from the transmitting antenna. In the plot, red indicates the strongest received signal and blue represents the weakest or no signal.

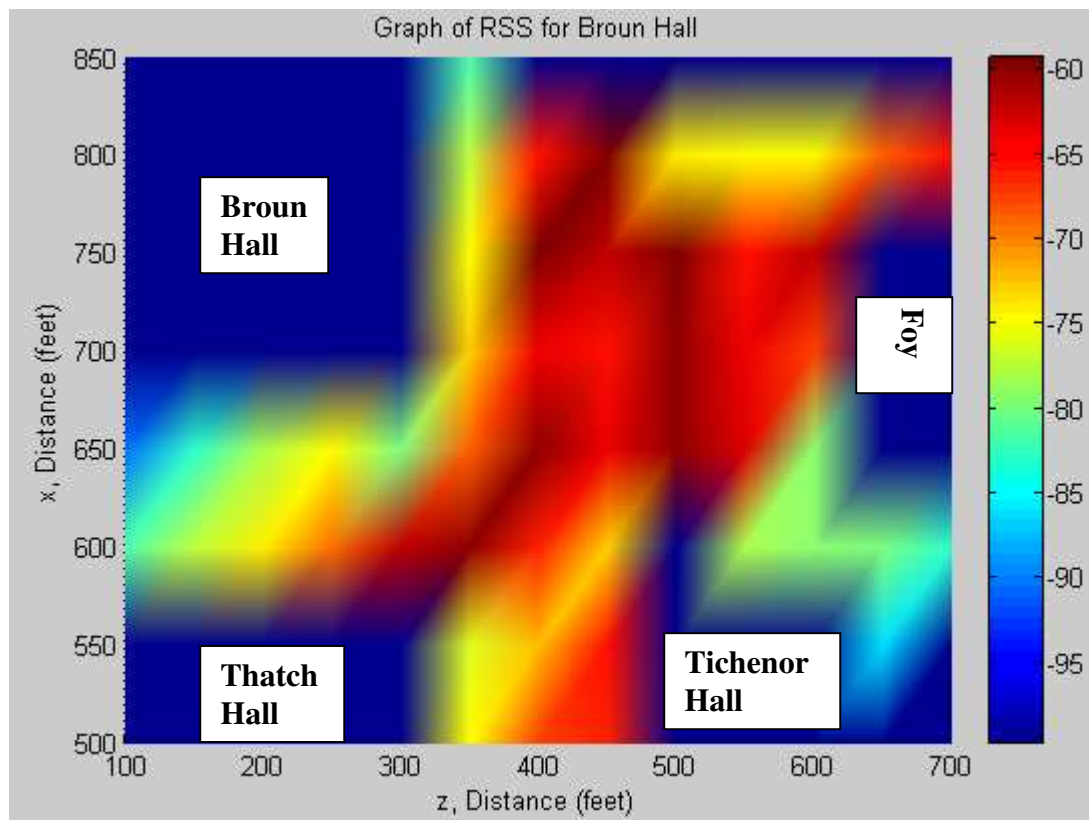


Figure 5.1: Variation of signal strength from Broun Hall's AP

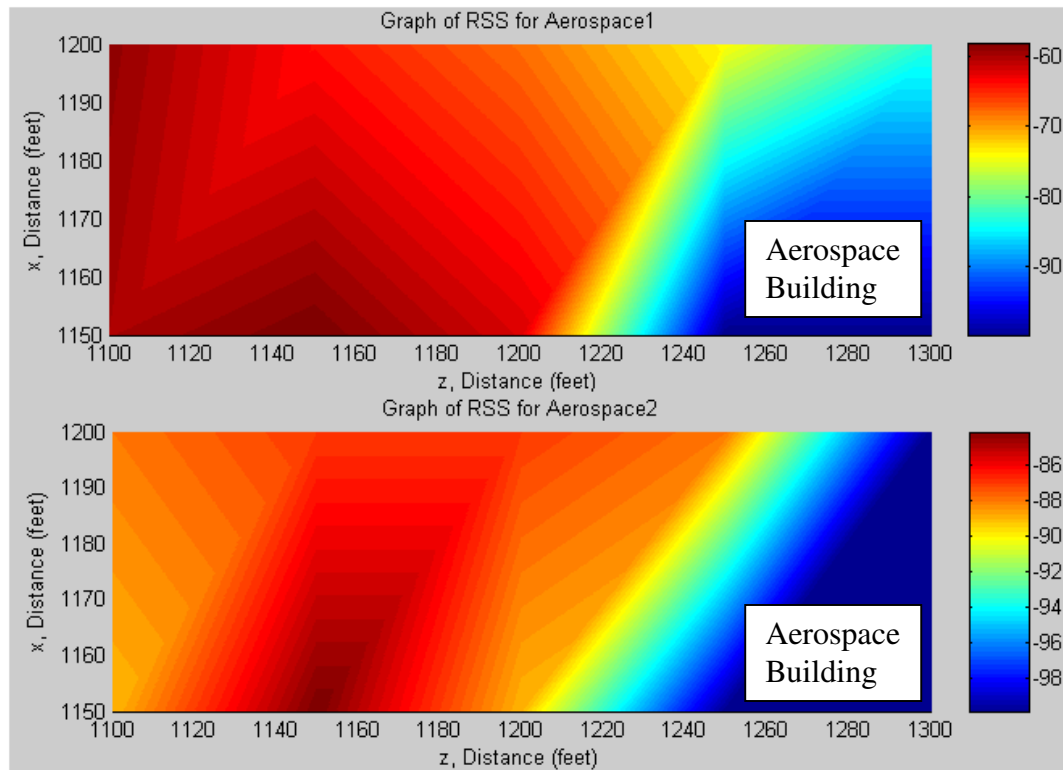


Figure 5.2: Variation of signal strength from the APs for Aerospace- APa1 (upper plot), APa2 (lower plot)

From Figures 5.1 and 5.2, there may have been coverage on the buildings' roofs but ENS was only interested in the ground coverage where most of the client's activity would be taking place.

It can be seen in the lower plot of Figure 5.2, that the signal strengths were not as high as those in the upper plot. This was because there was a loose connection that was later discovered.

5.3 BUILDING HEIGHTS TO PREDICT COVERAGE RANGE

The buildings' heights were obtained using a GPS instrument from Garmin. Measurements were taken at ground level (base of building) and at the top of the building where the AP was located to get the height of the AP. Table 5.1 shows the measurements.

Table 5.1: Buildings' height where the APs were located

Building	Building Height Average (ft)
<i>Broun Hall</i> Top (ft) Bottom (ft) Building Height (ft)	 700 637 63
<i>Dunstan Hall</i> Top (ft) Bottom (ft) Building Height (ft)	 700 668 32
<i>Aerospace</i> Building Height (ft)	 75

The inner and outer radius calculations were performed based on Figure 3.3 in Section 3.2.3. The vertical beamwidth, 40° was obtained from the SA24-120-9 antenna's data sheet. As mentioned before, A has to be greater than $BW/2$ so 20.5° was chosen to provide the minimum inner and maximum outer radii. These values are displayed in Table 5.2.

Table 5.2: Inner and outer radius calculations for the three APs based on [1]

Building	Antenna Height (ft)	Downtilt Angle (deg)	Inner Radius (ft)	Outer Radius (ft)	Covered Area (ft)²	Covered Area (km)
<i>Broun Hall</i>	63	20.5	52.8	7233.6	7180.8	2.2
<i>Dunstan Hall</i>	32	15.5	52.8	3643.2	3590.4	1.1
<i>Aerospace</i>	75	20.5	105.6	8606.4	8500.8	2.6

The empirical data in Figure 5.1 showed that the coverage range for the AP situated on Broun Hall was approximately 700 feet. This was not comparable to the theoretical value of 7180.8 feet. The calculation was done for an ideal environment devoid of scatters, interference, reflections, diffraction, that is perfectly flat (no terrain), no buildings, trees or other interferers in the propagation path. If the antenna mounted on the building had no downtilt and its main beam was radiating horizontally, then the coverage distance in the horizontal plane would have been greater than 700 feet and possibly closer to the theoretical value.

CHAPTER 6: A THEORETICAL ANALYSIS OF AP AND ANTENNA COVERAGE

In this section, a theoretical model is developed in order to compare predicted and measured E and H-plane radiation patterns based upon the manufacturer's measured data for the SA24-120-9 sectored antenna and the theoretical model developed. A further analysis is presented to estimate the ground coverage of the SA24-120-9 antenna. The analysis is based in part on measurements of the antenna's horizontal and vertical beamwidths, (120° and 40° respectively). Once the ground coverage is estimated, it will be compared to actual field measurements of the same.

6.1 USING MATLAB TO PLOT THE MANUFACTURER'S DATA

Figure 6.1 presents a Matlab plot of the radiation pattern in the horizontal, H-plane and vertical, E-plane based upon measured data provided by the antenna manufacturer.

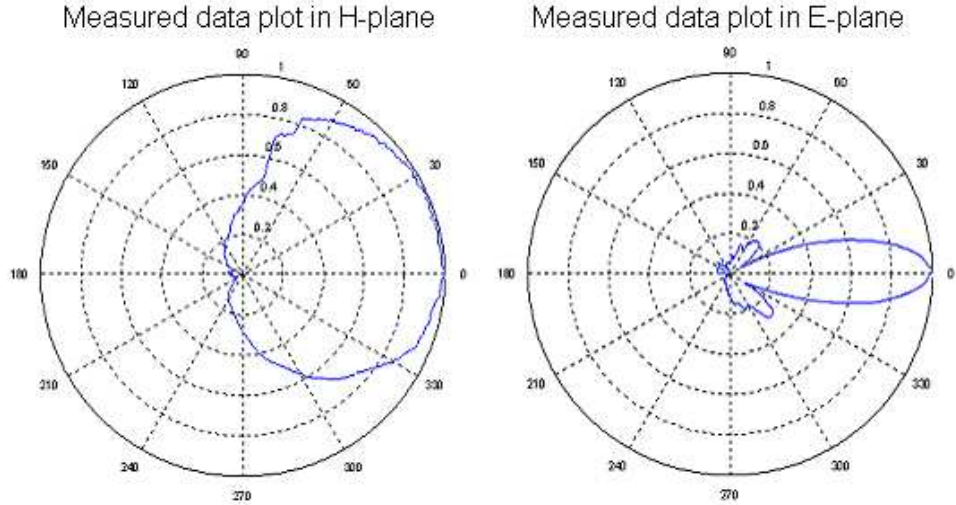


Figure 6.1: Polar plot generated in Matlab based on measured data for (a) H and (b) E-plane

6.2 DEVELOPING A THEORETICAL MODEL

A reasonable model of a far-field antenna pattern with a single major lobe [12] is

$$E = \cos^n(\theta)\cos(\phi)\hat{a}_\theta + \cos^m(\theta)\sin(\phi)\hat{a}_\phi \quad (6.1)$$

where $0 \leq \phi \leq 2\pi$ and $0 \leq \theta \leq \pi$. n and m are the powers of the cosine function that determine the beamwidth of the antenna pattern in the E and H-planes.

Assume the orientation in Figure 6.2.

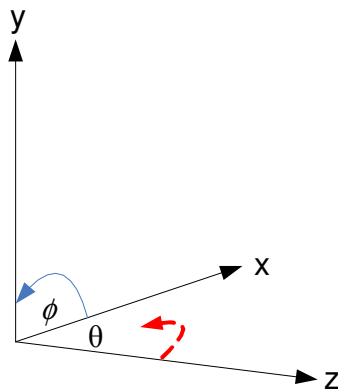


Figure 6.2: 3D Coordinate orientation for the analysis below

where y points vertically upwards, x is along the edge of the building (N-S) and z is horizontal and away from the building (E-W). In the z-y plane or E-plane cut where ϕ is 90° ,

$$E_\theta = \cos^m(\theta) \quad (6.2)$$

In the z-x plane or H-plane cut where ϕ is 0° ,

$$E_\phi = \cos^n(\theta) \quad (6.3)$$

Since the antenna pattern plots are normalized (maximum of unity) and the -3dB beamwidth is known to be 120° , n can be chosen to approximately match the measured data using

$$\cos^n(60^\circ) = 0.707 \quad (6.4)$$

resulting in $n = 0.5$. Similarly, to determine m for the vertical beamwidth, one may solve

$$\cos^m(15^\circ) = 0.707 \quad (6.5)$$

where $m = 10$.

Even though the data sheet quoted the antenna having a 40° vertical beamwidth, where one would expect to use $\cos^m(20^\circ) = 0.707$ to determine m, the measured data showed the antenna actually had a vertical beamwidth of approximately 30° . Hence, $\cos^m(15^\circ) = 0.707$ was used to determine m.

According to [13], the gain of an antenna with a single main lobe is given approximately by $G = \frac{41253}{HP_E HP_H}$. If one assumes that the gain and the half-power beamwidth in the H-plane are known (9dBi and 120° respectively for the antenna under study) then the HP_E must be 38° which is reasonably close to the 30° value quoted above.

As shown in Figure 6.3, E and H plane analytical pattern plots with $n = 0.5$ and $m = 10$ are compared with the measured data of Figure 6.1 and reasonably good agreement is observed.

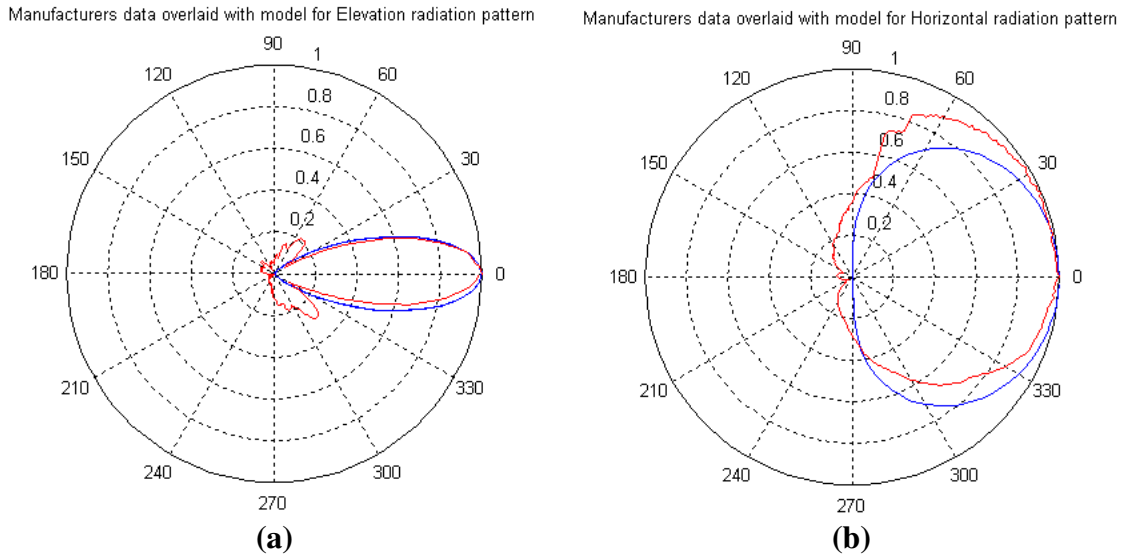


Figure 6.3: Manufacturer’s data (red) overlaid with the model (blue) for radiation patterns a) Elevation, m b) Horizontal, n

6.3 VERIFICATION TEST

Figure 6.4 is the basic measurement configuration that would be referenced throughout the rest of the chapter.

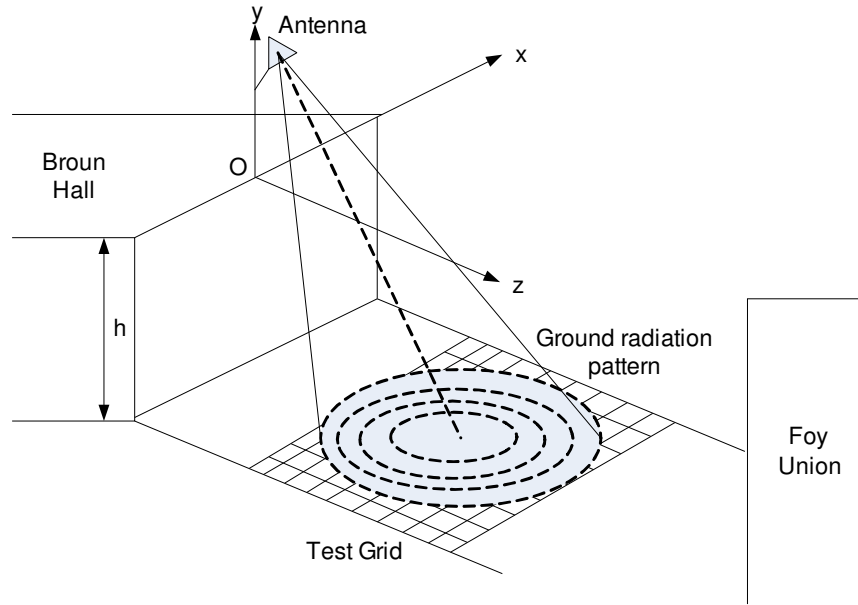


Figure 6.4: Coordinate system relative to exact geographic measurements

It was desirable to be assured that a vertical slice (parallel to the x-y plane) of the radiation pattern in the far-field produced concentric circles. Each term in the E-field function (equation 6.1) was squared so that contour plots of power density, P, could be produced resulting in

$$P = \cos^{2n}(\theta)\cos^2(\phi)\hat{a}_\theta + \cos^{2m}(\theta)\sin^2(\phi)\hat{a}_\phi \quad (6.6)$$

where n and m were both set to unity to verify that a vertical slice of the radiation pattern in the y-x plane produced these concentric circles. This contour was created at a distance of 200m from the building ($z = 200\text{m}$). The flow chart in Figure 6.5 shows the process used to create the plots in Figures 6.6 and 6.7.

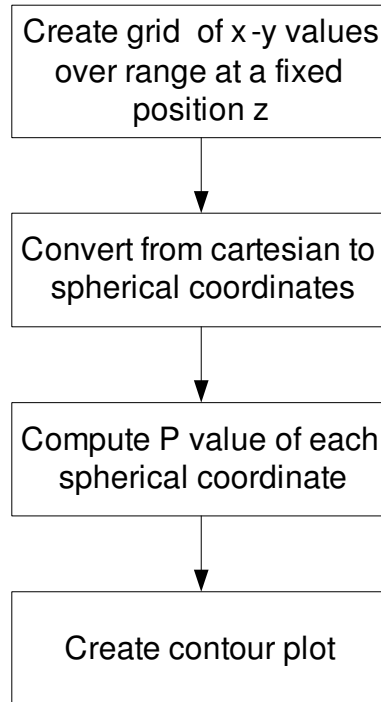


Figure 6.5: Process for creating Figures 6.6 and 6.7

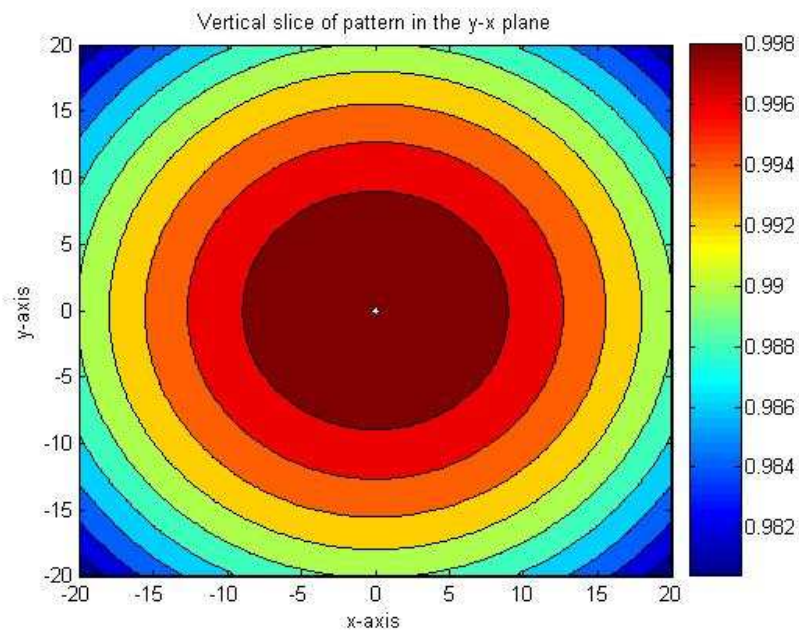


Figure 6.6: Contour plot of a radiation pattern with equal E and H-plane half power beamwidths

6.3.1 Contour Plots Of Far-Field Radiation Pattern For SA24-120-9 Antenna

The previously determined values of $m = 10$ and $n = 0.5$ were used in equation 6.6 and the theoretical contour antenna pattern is presented in Figure 6.7.

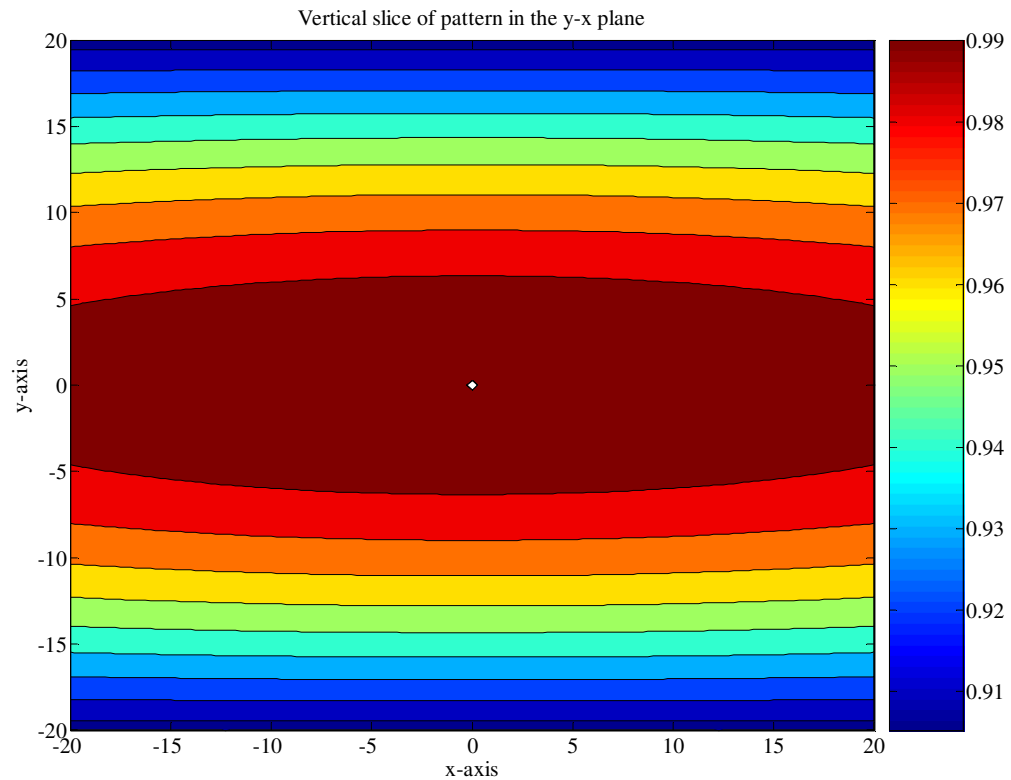


Figure 6.7: Contour of the antenna for field pattern

The elliptically shaped contours in Figure 6.7 are reasonable considering the value of n and m used. The minor axis of the ellipsis (z-y cut) is associated with the large exponent, $m = 10$, whereas the major axis of the ellipsis is associated with the small exponent $n = 0.5$.

6.4 COORDINATE ROTATION AND TRANSLATION

The next step in the analysis was to project the far-field antenna pattern into a plane parallel to the z-x plane corresponding to the test grid shown in Figure 6.4. This plane is 19.2m below the x-z plane in Figure 6.4. Furthermore, as shown in Figure 6.8 a coordinate system rotation about the x-axis of 20° was required to account for the antenna downtilt.

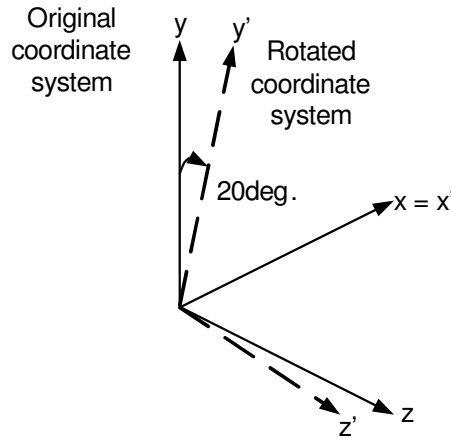


Figure 6.8: Comparing the original axes with the new ones after a 20° downtilt or rotation

For rotation about the x-axis, the rotational matrix is given by [3]

$$\begin{bmatrix} 1 & 0 & 0 \\ 0 & \cos\alpha & -\sin\alpha \\ 0 & \sin\alpha & \cos\alpha \end{bmatrix} \quad (6.7)$$

Relating the original coordinate system (x, y, z) relative to the rotated coordinate system (x', y', z') results in,

$$\begin{bmatrix} x \\ y \\ z \end{bmatrix} = \begin{bmatrix} 1 & 0 & 0 \\ 0 & \cos\alpha & -\sin\alpha \\ 0 & \sin\alpha & \cos\alpha \end{bmatrix} \begin{bmatrix} x' \\ y' \\ z' \end{bmatrix} \quad (6.8)$$

To get the new coordinates, the inverse of the rotational matrix would have to be multiplied by the old coordinate values resulting in

$$\begin{bmatrix} x' \\ y' \\ z' \end{bmatrix} = \begin{bmatrix} 1 & 0 & 0 \\ 0 & \cos\alpha & \sin\alpha \\ 0 & -\sin\alpha & \cos\alpha \end{bmatrix} \begin{bmatrix} x \\ y \\ z \end{bmatrix} \quad (6.9)$$

Translation was a simple procedure whereby 19.2 was subtracted from each y-value in a particular range in Matlab. Essentially, the z-x plane was moved from parallel to the building's roof to ground level. The remaining procedure follows the method described in Figure 6.5.

It was hypothesized that the antenna's contour pattern when projected onto the ground would consist of a small segment of concentric ellipses. It can be seen from Figure 6.9 that the hypothesized result is in reasonable agreement with the simulated results.

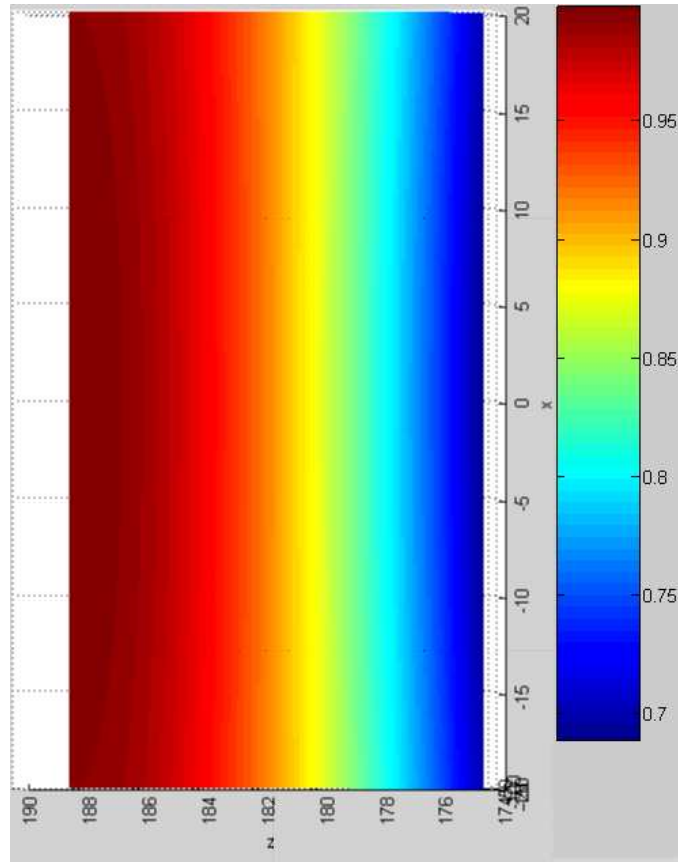


Figure 6.9: Ground plot after translation and rotation

6.5 COMPARING THE ANALYTICAL AND MEASURED PLOTS

Finally, it was of interest to compare the antenna's theoretical ground coverage with the measured data. The theoretical pattern data was developed without taking into account reflections from nearby buildings. Hence, as shown in Figure 6.9 the results were perfect x-directed lines.

At 200 feet from Broun Hall, where one would now examine the radiation patterns at 300 feet and beyond, there were no obvious half ellipses seen. The wireless channel is considered random since the signals between the transmitter and receiver are not propagating in an ideal LOS environment. There are impairments that cause the signal to vary during transmission like reflections, diffraction and multipath interference. In

addition, there were buildings and benches impeding the signal propagation so the smooth curves in Figure 6.9 could not be achieved. As a result, the plots in Figures 6.9 and 6.10 do not look alike.

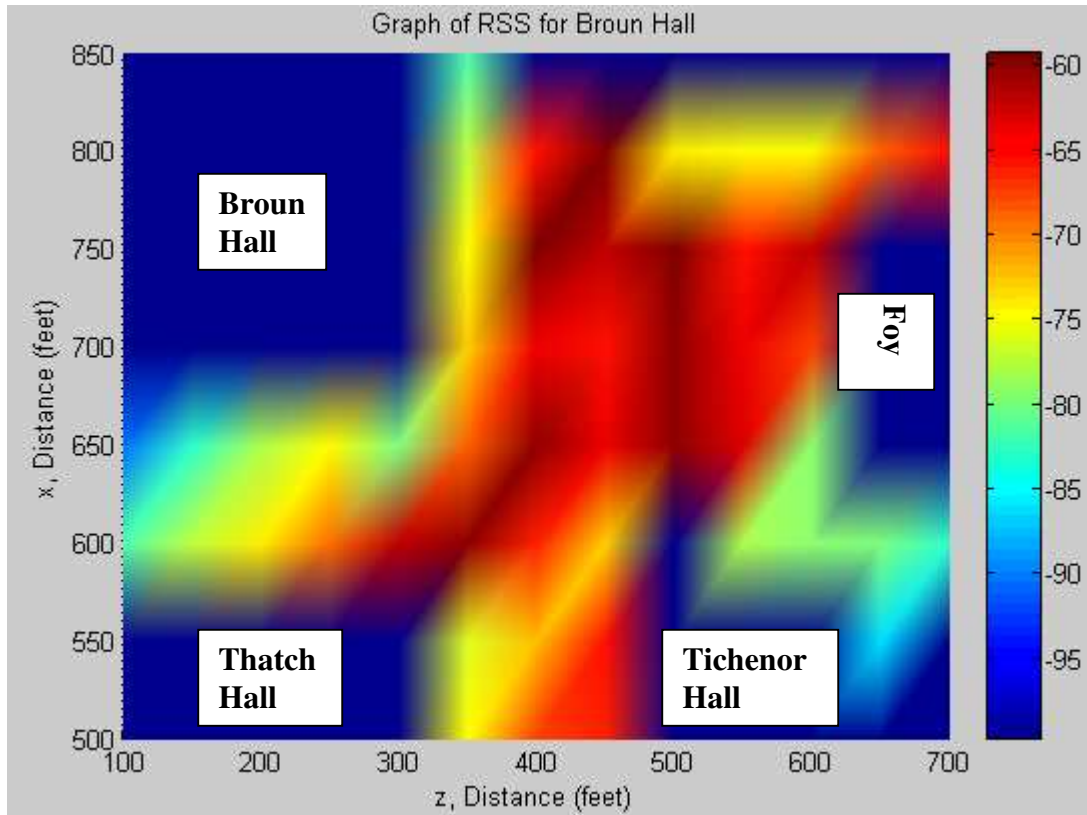


Figure 6.10: Empirical results for Broun Hall antenna's ground coverage

CHAPTER 7: ANTENNA ANALYSIS: CREATING THE RADIATION PATTERNS FOR THE CELLULAR ANTENNA

It was not feasible to open and examine the contents of the AP antenna (SA24-120-9) discussed in the previous chapter. An improvisation was made whereby an existing cellular base-station antenna, PCSS090-10-0 (Figure 7.1) from CSA Wireless was available that already exposed its six microstrip patches and interconnecting transmission lines, T-lines.

In this chapter, a theoretical approach is presented to analyze a cellular antenna's E- and H-plane radiation patterns. Once the theoretical model is created, the radiation patterns obtained are then compared to those in the data sheet of the PCSS090-10-0.

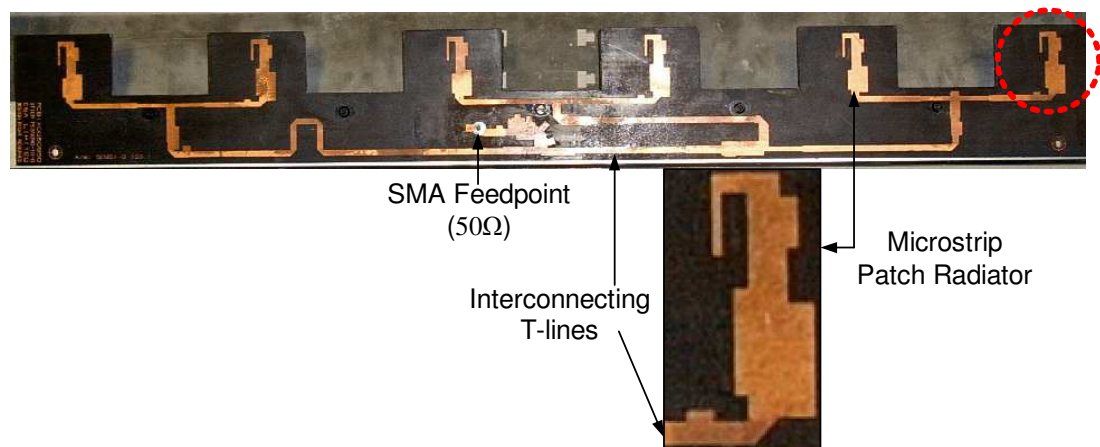


Figure 7.1: PCSS090-10-0 6-element microstrip patch antenna

7.1 BACKGROUND

The technique of determining the far-field pattern of an array of identical microstrip patches or antenna elements is referred to as *Pattern Multiplication* [13]. To obtain the antenna's overall far-field E-plane radiation pattern, the single microstrip patch function in the E-plane has to be multiplied by the corresponding array factor function in the E-plane. The array factor is simply the pattern due to an array of isotropic point sources located at the center of each microstrip patch element. Furthermore, each isotropic point source must have the same amplitude and relative phase as its corresponding microstrip patch element. The principle of pattern multiplication can also be used to determine the final H-plane radiation pattern.

In conducting the analysis, some assumptions have to be made. The array is linear, ie. the antenna patches are evenly spaced along a line. Furthermore, it is assumed that each antenna element has equal magnitude excitation. Figure 7.2 provides the coordinate system relative to the antenna's orientation that is used to determine the principal plane pattern functions.

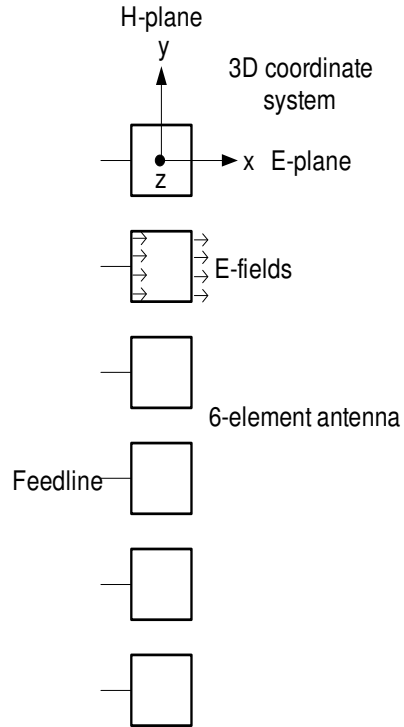


Figure 7.2: 3D coordinate system for PCSS090-10 antenna

7.2 DETERMINING THE SINGLE ELEMENT FUNCTIONS

As derived in reference [13] the microstrip element E-plane (x-z cut) and H-plane (y-z cut) is given by

$$F_e(\theta) = \cos\left(\frac{\beta L}{2} \sin \theta\right) \quad \text{E-plane, } \phi = 0^\circ \quad (7.1)$$

and

$$F_h(\theta) = \cos\theta \frac{\sin\left[\frac{\beta W}{2} \sin \theta\right]}{\frac{\beta W}{2} \sin \theta} \quad \text{H-plane, } \phi = 90^\circ \quad (7.2)$$

where $\beta = \frac{2\pi}{\lambda}$ is the free-space phase constant (λ = the free space wavelength) and for the

analysis, a square patch is assumed, $L = W = \frac{0.5\lambda}{\sqrt{\epsilon_r}}$. According to the manufacturer of

the PCSS090-10-0, the dielectric constant of the high frequency laminate upon which the patch elements are printed is $\epsilon_r = 2.5$.

7.3 DETERMINING THE ARRAY FACTOR FUNCTION

As mentioned above far-field radiation pattern resulting from an array of identical isotropic point sources fed with the same amplitude and with a linear phase progression is referred to as the array factor. Specifically the array pattern is given by

$$F(\theta) = \frac{\sin\left(\frac{N\psi}{2}\right)}{N \sin\left(\frac{\psi}{2}\right)} \quad (7.4)$$

where

$$\psi = \beta d \cos\theta + \alpha \quad (7.5)$$

with β being the free space phase constant (previously defined), α is the linear phase taper along the array and N is the number of elements (6 in this case). Since all the patch elements are in phase, $\alpha = 0$. One can observe from Figure 7.1 that the length of T-line from the feed point to each element is the same. Therefore, each element is in-phase and $\alpha = 0$. Substituting the values provided above into equation 7.5 yields

$$F(\theta) = \frac{\sin(6\pi \sin \theta)}{6 \sin(\pi \sin \theta)} \quad (7.6)$$

for the H-plane array pattern.

In the E-plane cut where $\phi = 0^\circ$, the array factor is unity due to the isotropic nature of the microstrip patch.

7.4 CORRECTION FACTOR

A function, correction factor representing a cardioid shape is multiplied by the array factor in order to “round-off” the back lobes. The correction factor can be justified based on the equivalence principle that leads to trigonometric functions that multiply the radiation integrals (sometimes referred to as obliquity factors). In this case, the correction factor or obliquity factor is

$$\frac{1}{2}(1+\cos\theta) \quad (7.7)$$

7.5 RESULTS OF PATTERN MULTIPLICATION

The following plots illustrate the principle of pattern multiplication and the result of using this technique to obtain the complete H- and E-plane patterns. As indicated in Figure 7.3, the complete H-plane pattern (Figure 7.3d) is the product of the patterns shown in Figure 7.3a, Figure 7.3b and Figure 7.3c which are respectively the H-plane element pattern, array factor and correction factor (obliquity factor). Finally, Figure 7.3d compares the analytically computed pattern to the manufacturer’s measured pattern and it is seen that reasonably good agreement is obtained especially considering the simplicity of the analysis approach.

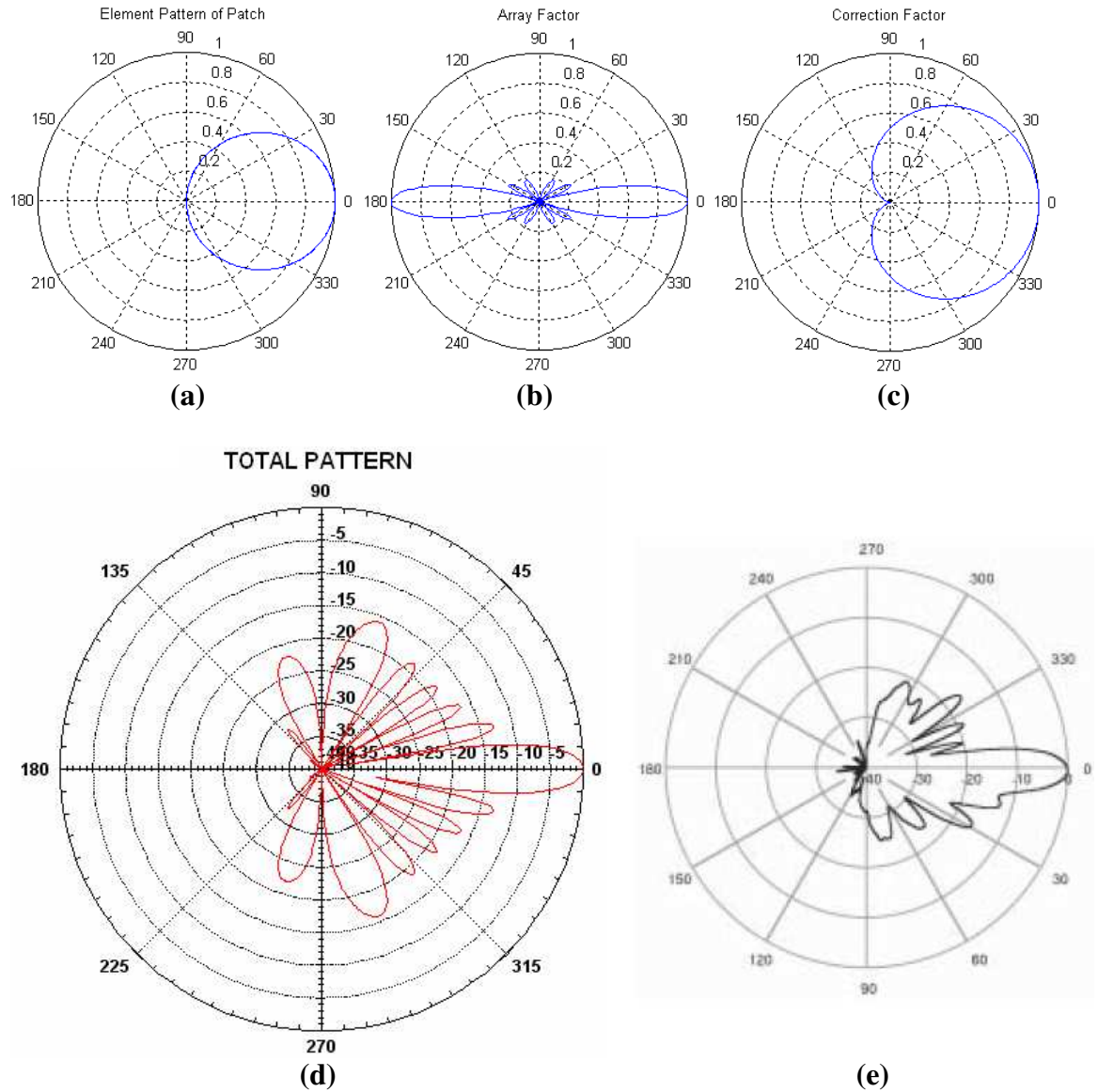


Figure 7.3: H-plane pattern multiplication

Figure 7.4 presents the pattern analysis for the E-plane. In particular Figure 7.4d is the result of the product of the element pattern (Figure 7.4a), array factor (isotropic in this cut, Figure 7.4b), and obliquity factor (Figure 7.4c). Due to problems in Matlab when generating the pattern multiplication result in a decibel form, Harvard Chart XL was used to generate the resultant polar plot.

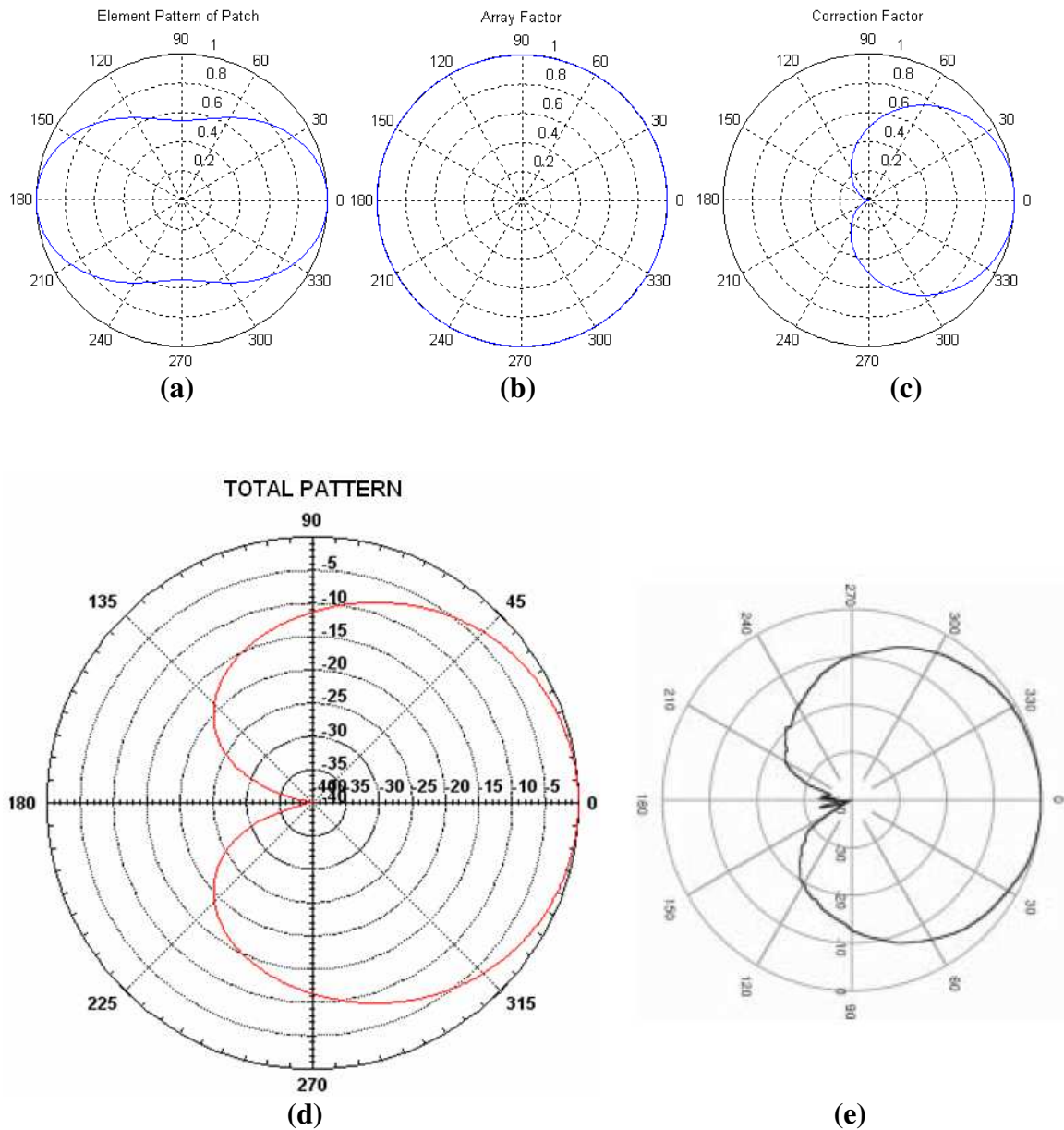


Figure 7.4: E-plane pattern multiplication

One can observe that relative to the H-plane pattern, the E-plane pattern is relatively broad. Once again comparing Figure 7.4d and 7.4e reasonable good agreement is observed between the measured and E-plane predicted pattern. Figure 7.4d was generated using the Harvard Chart XL program.

CHAPTER 8: GENERAL ANALYSIS OF THE INPUT IMPEDANCE CHARACTERISTIC

8.1 BACKGROUND

Chapter 8 continues with the analysis of the PCSS090-10-0 cellular antenna. The objective of this section is to conduct a general analysis of the input impedance characteristic of the base station antenna. A single microstrip patch identical to the one used on the PCSS090-10-0 was built and analyzed in an attempt to gain a more complete understanding of how the input impedance of a single isolated patch was related to the same for the six-patch antenna. As indicated in Figure 8.1, a Hewlett Packard Vector Network Analyzer (8753-C) was used to measure the input impedance to the antenna. The measurement was repeated with the antenna inserted half-way into its radome. Measurements with and without the radome are presented in Figures 8.3 and 8.6 and Figures 8.4 and 8.7 respectively. Furthermore, the analyzer was programmed to display the Voltage Standing Wave Ratio (VSWR) and Smith Chart plots over the range of frequencies from 1500 to 2200MHz. According to the manufacturer's data sheet, the antenna is designed to operate with acceptably low VSWR over the range of frequencies from 1850 to 1990MHz.

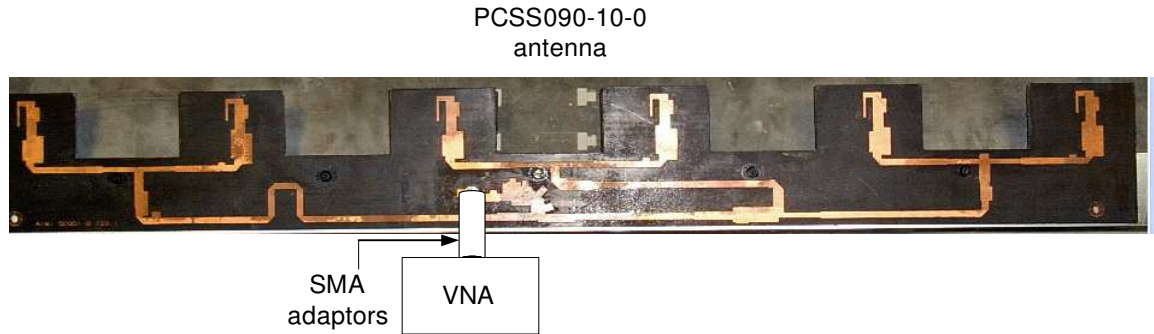


Figure 8.1: PCSS090-10-0 antenna connected to VNA

8.2 ANALYZING THE PCSS090-10-0 ANTENNA

8.2.1 Using The VNA

The VNA is used to measure the VSWR of the base station antenna when it is connected to the analyzer. Before any antenna measurements are made, the VNA was calibrated with the following standard terminations, short circuit, open circuit and a 50Ω matched load by manually connecting them to the test ports of the VNA. Figure 8.2 shows a VSWR plot for a matched load being connected to the VNA terminal. The VSWR of 1.053:1 proved that the calibration is sound as there are negligible reflections at the load.

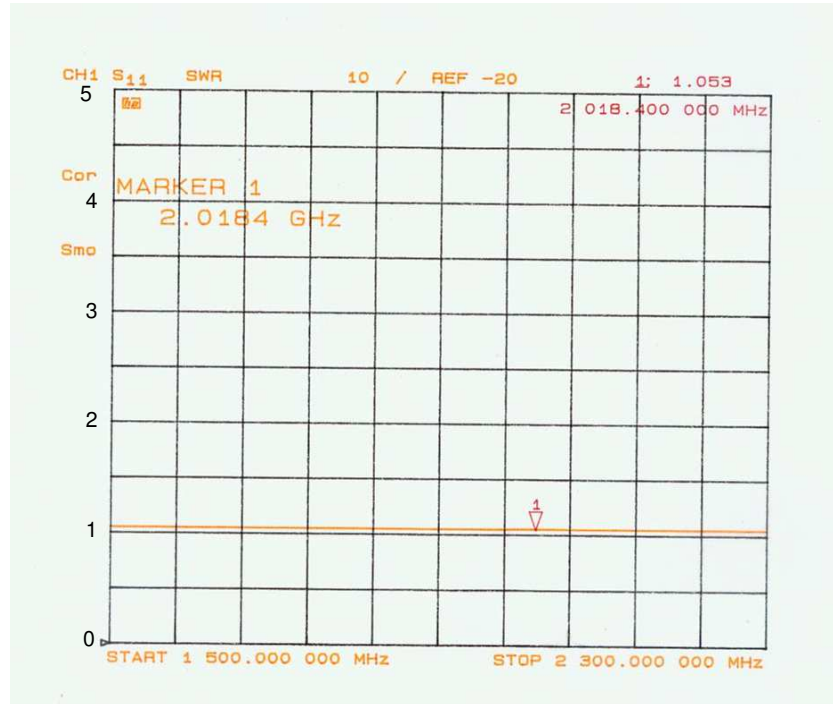


Figure 8.2: VSWR vs. Frequency for a matched load

According to the manufacturer's data sheet [2], the PCSS090-10-0 operating range is 1850MHz to 1990MHz. Figure 8.3 displays a plot of VSWR versus frequency which highlights the VSWR at the upper and lower frequency bounds and at the minimum point of the plot. This measurement is conducted on the actual antenna when it is in its fiber-glass casing or radome. Due to the SMA connector soldered to the antenna, only half of the antenna was enclosed while the other half was exposed to air.

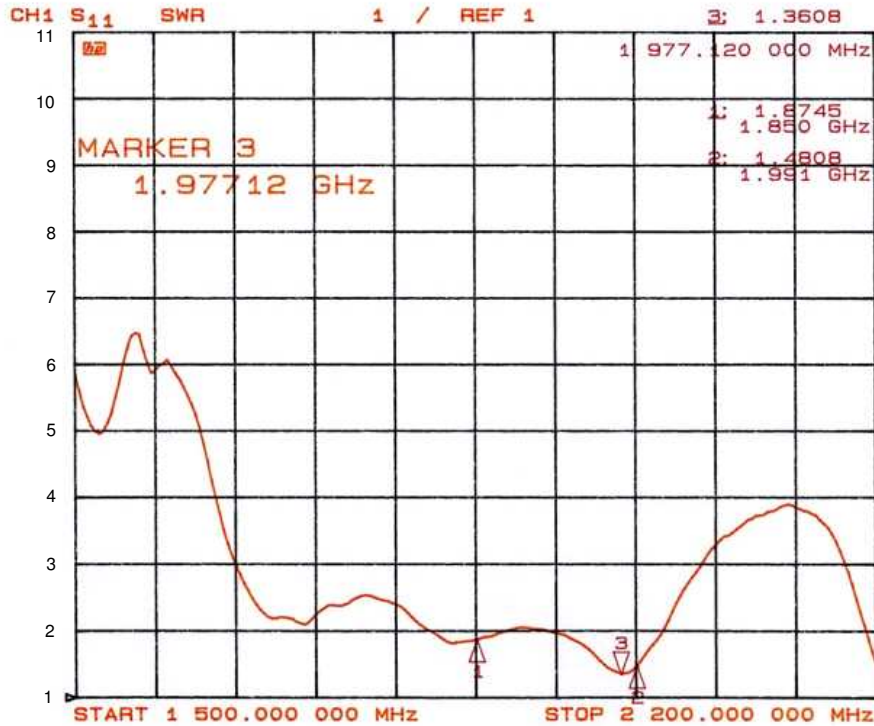


Figure 8.3: VSWR vs. Frequency for the PCSS090-10-0 antenna inside radome

One can see from Figure 8.3 that at the minimum point of the plot (data marker 3) which occurs at 1.97712GHz, the VSWR is 1.36:1. According to the manufacturer, the VSWR should be less than 1.4:1 so there was good correlation between the manufacturer's specifications and measurements. Since the VSWR of 1.36 is fairly close to 1, the antenna is reasonably well matched to the 50Ω characteristic impedance (Z_0) of the feed line. The VSWR at the upper frequency bound (approximately 1.45:1) indicates that there is better matching at the high end of the band than at the lower frequency bound where the VSWR is approximately 1.8:1.

The next step in the analysis was to examine the behavior of the antenna when outside its radome.

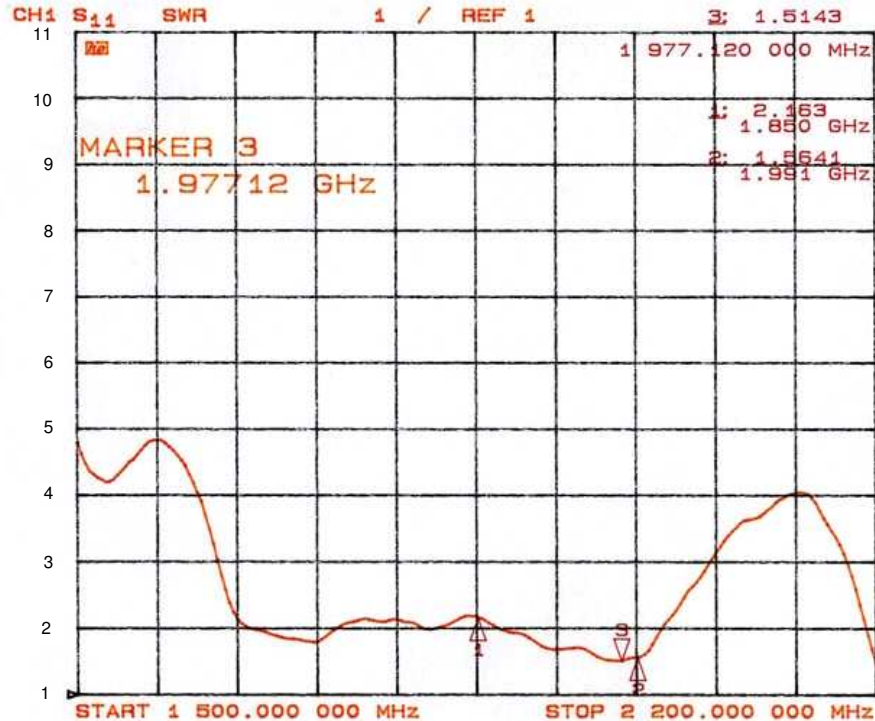


Figure 8.4: VSWR vs. Frequency for the PCSS090-10-0 antenna outside radome

Examining Figure 8.4 and comparing it to Figure 8.3 the lower frequency bound and the upper frequency bound corresponds to a VSWR of approximately 2.2:1 and 1.55:1. Since the VSWR values when the antenna is outside its radome are slightly higher than those when the antenna is half-way in its radome, one can definitively conclude that the antenna is better matched when inside the radome.

8.3 BUILDING THE MICROSTRIP PATCH AND CONDUCTING MEASUREMENTS

A piece of double-sided copper RT Duroid 5880 board with a dielectric constant of $\epsilon_r = 2.2$ was used to construct a single microstrip patch identical to those used in the PCSS090-10-0 antenna. The single antenna's dimensions and parameters are taken from

one of the patches shown in Figure 8.1. Figure 8.5a shows the microstrip antenna after etching. On the backside of the board, a SMA connector was soldered (Figure 8.5b) to make an edge-fed connection to the VNA. This patch antenna will be referred to as the “commercial board antenna”.

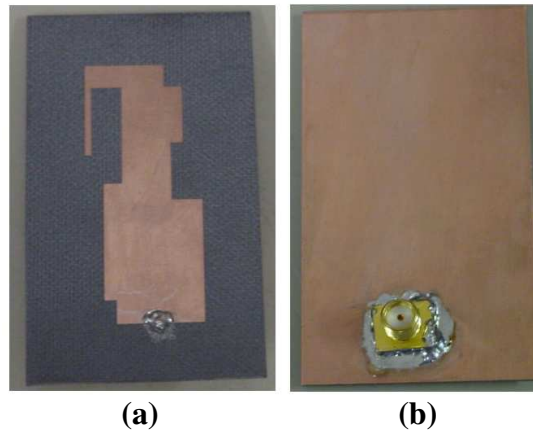


Figure 8.5: (a) Fabricated patch based upon commercial cellular patch (b) SMA connector used to provide an edge-feed to the patch

8.4 SMITH CHART ANALYSIS

In the upcoming section Smith Chart plots will be presented for the commercial board antenna and the PCSS090-10-0 antenna to have a deeper understanding of the role of a single microstrip patch in the array with respect to input impedance (Figure 8.8). The effects of the radome (Figures 8.6 and 8.7) on the input impedance will also be presented. The analysis will be based on the bandwidth bounds (1850MHz to 1990MHz) of the frequency range stated by the PCSS090-10-0 manufacturer.

Once the VNA is calibrated, the commercial board antenna or the PCSS090-10-0 antenna is connected directly to the test port. The VNA was programmed to display a Smith Chart and additionally markers were used to indicate the lower and upper operational frequency bounds.

8.4.1 Smith Chart Of PCSS090-10-0 Antenna

Figure 8.6 is the Smith Chart plot for the PCSS090-10-0 cellular antenna. One can obviously see that the input impedance ($42.658-j15.951\Omega$) at the upper frequency is reasonably close to the characteristic impedance of 50Ω (origin of the Smith Chart). Though the input impedance at the lower frequency, $37.703-j25.363\Omega$ is not exactly 50Ω , it still results in a VSWR less than 2:1.

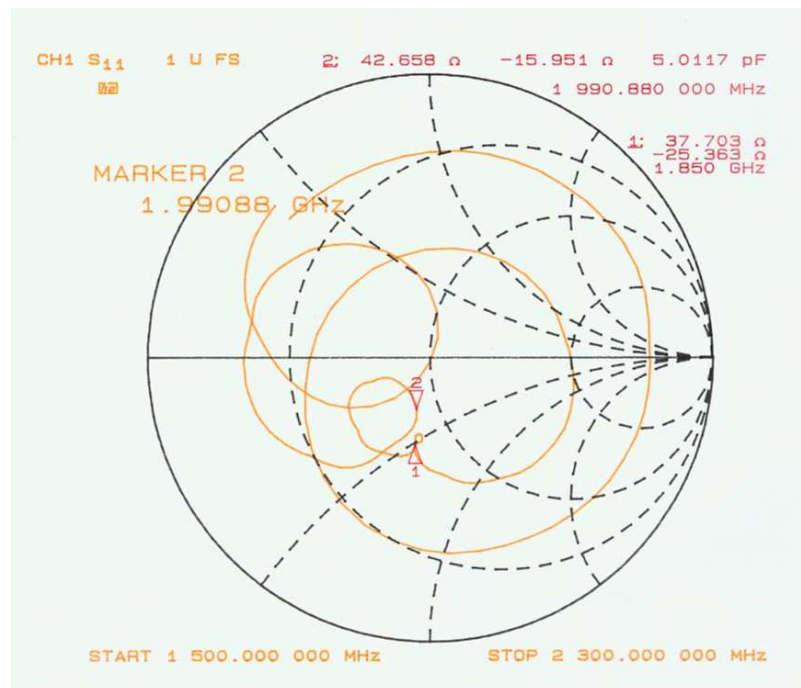


Figure 8.6: Smith Chart of PCSS090-10-0 outside radome

For an ideal matched network, the aim is to move to the center of the Smith Chart where the reflection coefficient is zero and the input impedance to the microstrip patch is purely real and equal to the characteristic impedance of the feedline. Figure 8.7 shows the Smith Chart plot when the radome is held parallel to the array and moved a few inches back and forth in front of the array. It is evident that both markers did move closer to the

origin of the Smith Chart indicating that a better match is probably achieved with the array inserted into the radome.

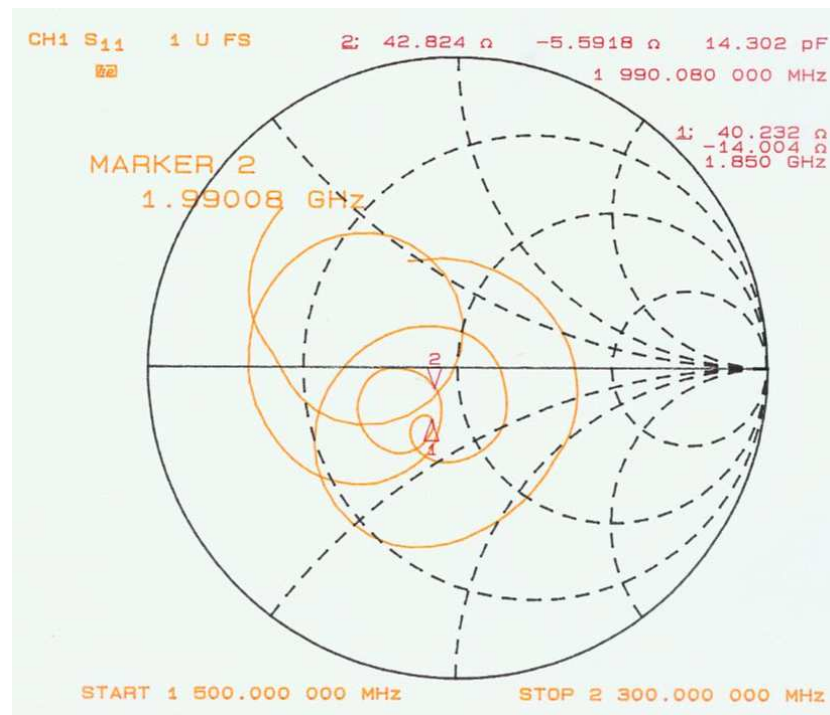


Figure 8.7: Smith Chart of PCSS090-10-0 inside radome

It should be noted that during this test, the input impedance measurements were fluctuating between 42Ω to 49Ω due to the fact that the radome could not be held perfectly still or perfectly parallel to the array. This human error caused the impedance value to be recorded as 42.824-j5.5918Ω at the upper frequency bound. Overall, however, this result further supports the fact that the antenna array is better matched with the radome than without it.

8.4.2 Commercial Board Antenna Smith Chart

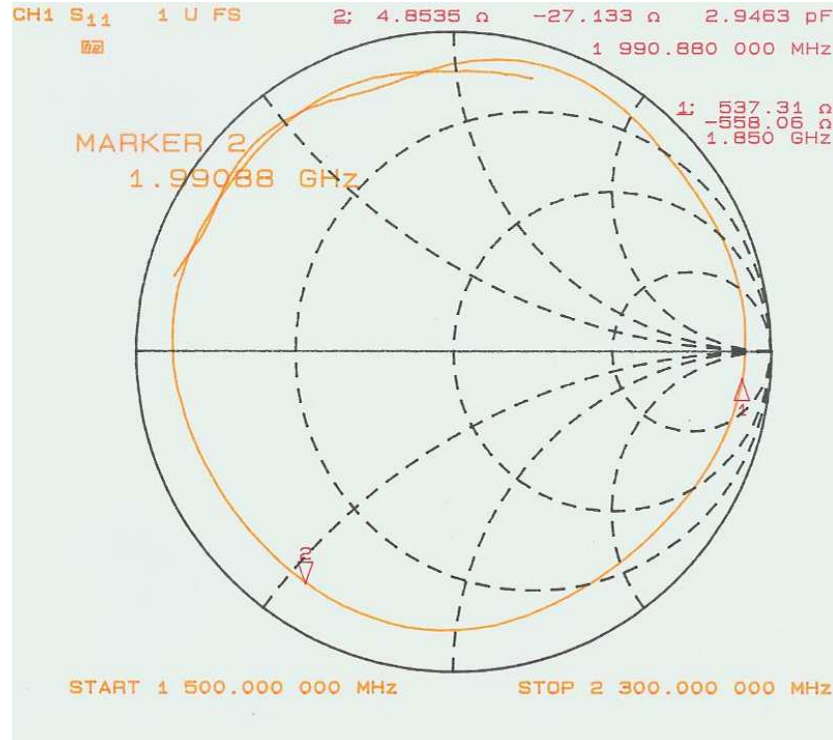


Figure 8.8: Smith Chart of commercial board antenna

Examining the Smith Chart in Figure 8.8, one may observe that all possible input impedances over the range of frequencies specified by the manufacturer are captured within the arc between markers. At the upper frequency bound, the load impedance is $Z_L = 4.8535 - j27.133 \Omega$ and at the lower frequency bound it is $Z_L = 537.31 - j558.06 \Omega$. A matching network will be needed in addition to the microstrip patch in order to transform the input impedance from each patch over this range of frequencies to the center of the chart.

8.5 COMPARING A THEORETICAL VALUE OF IMPEDANCE TO THE MEASURED VALUE

According to [13], an approximate expression for the input impedance of an edge-fed patch is given by

$$Z_A = 90 \frac{\epsilon_r^2}{\epsilon_r - 1} \left(\frac{L}{W} \right) \Omega \quad (8.1)$$

where the dimensions of the patch are, length, $L = 4.5\text{cm}$, width, $W = 1.9\text{cm}$ and the dielectric constant of the commercial board antenna's substrate is 2.2 leading to $Z_A = 2.04\text{k}\Omega$. For $L > W$, a high value of input impedance looking into the single patch is expected. On the plot of Figure 8.8, at the upper frequency bound, the input impedance is 775Ω . This is a high value but not comparable to the theoretical value of $2.04\text{k}\Omega$. The difference in results is attributed to the fact that the theoretical analysis is based on a rectangle with length, L and width, W . Considerations were not made for the irregular-shaped PCSS090-10-0 patch.

8.6 SUMMARY

The commercial board antenna represents a single microstrip patch of the PCSS090-10-0 antenna. When placed in the array with the other five elements with matching networks while in the presence of the radome, the overall input impedance is near 50Ω . The matching of the actual patches to the input transmission line on the PCSS090-10-0 antenna is made by adjusting the widths of the T-line connecting the patches to the common feed point and by inserting stubs of various positions along the interconnecting

lines (see Figure 8.9). The matching networks used may have been open or short circuit shunt stubs which were in form of irregular shaped protrusions or variable line widths.



Figure 8.9: Examples of matching alterations

It should also be noted that based on the transmission line layout in Figure 8.1, by the process of dividing resistance in parallel and moving from the input impedance of a single patch to the overall impedance of the antenna, assuming all the PCSS090-10-0 patches are the same, the impedance looking into the six-element antenna is close to 50Ω as stated by the manufacturer and proven by measurements based on Figure 8.7.

CONCLUSION

There are many factors that affect the propagation of radio signals and no one model can accurately account for all factors. Existing theoretical models were used to compute signal attenuation and predicted values were compared to measured data to determine which model best represents the operating environment of the WLAN. All the models tested were in fairly good agreement with the measured data. The best performing model was the one that incorporated the most environmental factors.

In designing the WLAN, once the network designer decides where the hardware is to be positioned to obtain maximum coverage, appropriate equipment and cabling can then be chosen based on performance and how conveniently the hardware can be intergrated into the existing network. The “text-book” design that was done, worked perfectly when physically implemented. Ultimately, when the entire system is completely installed and configured, the true performance test will be if the wireless and wired system can co-exist with no problems.

A wireless network does not have the level of security as its wired counterpart. Besides using SSID’s and VPN’s, Cisco’s Clean Access suite is implemented in the AU wireless network.

Once the APs and antennas were configured and mounted on the buildings, signal strength readings were recorded and Matlab plots created to provide a graphical

representation of the coverage provided by the APs on Broun Hall and the Aerospace building. A theoretical analysis was conducted based on manufacturer's data to estimate the ground coverage of the SA24-120-9 antenna. This theoretical model was then compared with actual field measurements. During the analysis, it was discovered that the manufacturer's data sheet plots did not match the measured data they supplied. Due to the on-campus construction, the number of data points collected was limited because of restricted access areas. More data would definitely have given a better representation of the coverage area.

A theoretical approach of pattern multiplication was used to recreate the E- and H-plane radiation cuts of the PCSS090-10-0 cellular antenna. The models developed were compared with the corresponding E and H planes stated by the manufacturer and there was reasonable similarity between them.

The antenna when examined inside and outside its radome and measurements indicated that it was more closely matched to a 50Ω characteristic when inside the radome. A single microstrip element identical to those used in the array was built and its input impedance measured. Because the patch's length to width ratio is small, its input impedance is large and the T-lines and stubs on the actual antenna were designed to reduce the combined high input impedance of each element to approximately 50Ω .

RECOMMENDATIONS

The network designer could consider a device that is multi-functional. For example, while performing its primary function, acting as a wireless AP, the device could also have built in switch and router functionality. Once this proposed device is configured correctly, it could introduce hardware redundancy where the wireless network connects to the wired backbone which can be advantageous to the overall system.

The PoE and AP were two separate units in the establishing of the antenna and AP connection to the wired backbone (Figure 3.9). One device could be used for both purposes and this might reduce cost by minimizing cabling requirements and also a single unit would occupy less space. For example, with integrated IEEE 802.3af PoE, the ProCurve Wireless Access Point 420 offers a cost-effective means to deploy either an 802.11b or 802.11g wireless network.

Using devices that implement Multiple Input-Multiple Output (MIMO) technology can help improve the network's overall performance regarding capacity and coverage. The use of two or more antennas, along with the transmission of multiple signals (one for each antenna) at the source and the destination might help eliminate problems caused by multipath wave propagation [16]. The compromise with such a system is the additional costs incurred with installing more antennas at both the transmitter and the receiver. The long term effects would be beneficial since "a properly-designed MIMO system can

increase effective coverage by up to eight times and simultaneously deliver up to six times greater effective throughput” [15].

REFERENCES

- [1] Downtilt Coverage Radius, www.terabeam.com
- [2] PCSS090-10 data sheet, www.csa-wireless.com
- [3] Rotational Matrices, www.euclideanspace.com
- [4] IEEE 802.3af, www.answers.com/topic/802-3af
- [5] “Selecting Channel Frequencies for Wireless APs”, www.technet2.microsoft.com
- [6] “Channel Deployment Issues for 2.4GHz 802.11 WLANs”, www.cisco.com
- [7] Stuart M. Wentworth, *Fundamentals Of Electromagnetics With Engineering Applications*, Wiley, 2005
- [8] “Fulfilling the requirements of wireless networks for the enterprise”, www.csgcorp.com
- [9] Clint Smith, *Practical Cellular & PCS Design*, McGraw-Hill, 1998
- [10] Theodore S. Rappaport, *Wireless Communications Principles and Practices*, 2e, Prentice Hall, 2002
- [11] “University of Georgia Upgrades Celebrated Wireless Research Network with BelAir Networks Wide-Area Wi-Fi Infrastructure”, www.bbexchange.com
- [12] Dr. Riggs, Professor, Auburn University
- [13] Warren L. Stutzman, Gary A. Thiele, *Antenna Theory and Design*, 2e, Wiley, 1998
- [14] “Cisco Clean Access Manager Installation and Administration Guide”, www.cisco.com
- [15] “MIMO's multi-dimensional approach multiplies capacity”, www.commsdesign.com

[16] MIMO, www.whatis.com